Thiolate *versus* Selenolate: Structure, Stability, and Charge Transfer Properties

Jakub Ossowski,[†] Tobias Wächter,[‡] Laura Silies,[§] Martin Kind,[§] Agnieszka Noworolska,[†] Florian Blobner,[∥] Dominika Gnatek,[†] Jakub Rysz,[†] Michael Bolte,[§] Peter Feulner,[∥] Andreas Terfort,[*,§] Piotr Cyganik,[*,†] and Michael Zharnikov[*,‡]

[†]Smoluchowski Institute of Physics, Jagiellonian University, Reymonta 4, 30-059 Krakow, Poland, [‡]Angewandte Physikalische Chemie, Universität Heidelberg, Im Neuenheimer Feld 253, 69120 Heidelberg, Germany, [§]Institut für Anorganische und Analytische Chemie, Universität Frankfurt, Max-von-Laue-Straße 7, 60438 Frankfurt, Germany, and [∥]Physikdepartment E20, Technische Universität München, 85747 Garching, Germany

ABSTRACT Selenolate is considered as an alternative to thiolate to serve as a headgroup mediating the formation of self-assembled monolayers (SAMs) on coinage metal substrates. There are, however, ongoing vivid discussions regarding the advantages and disadvantages of these anchor groups, regarding, in particular, the energetics of the headgroup–substrate interface and their efficiency in terms of charge transport/transfer. Here we introduce a well-defined model system of 6-cyanonaphthalene-2-thiolate and -selenolate SAMs on Au(111) to resolve these controversies. The exact structural arrangements in both types of SAMs are somewhat different, suggesting a better SAM-building ability in the case of selenolates. At the same time, both types of SAMs have similar packing densities and molecular orientations. This permitted reliable competitive exchange and ion-beam-induced desorption experiments which provided unequivocal evidence for a stronger bonding of selenolates to the substrate as compared to the thiolates. Regardless of this difference, the dynamic charge transfer properties of the thiolate- and selenolate-based adsorbates were found to be nearly identical, as determined by the core–hole–clock approach, which is explained by a redistribution of electron density along the molecular framework, compensating the difference in the substrate–headgroup bond strength.

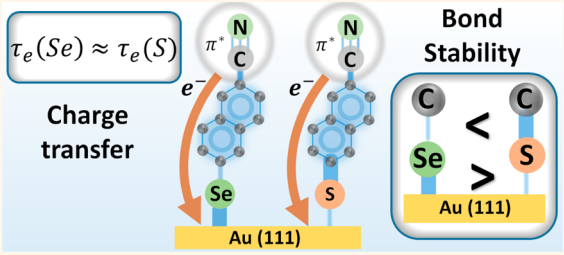

KEYWORDS: selenolate · self-assembly · self-assembled monolayers · charge transfer · bond strength · metal surfaces

Self-assembled monolayers (SAMs) are an indispensable playground of surface science and physical chemistry of interfaces as well as an important element of modern nanotechnology.[1−3] Numerous applications of these systems rely on the flexible molecular design of their constituents involving, in its turn, a suitable combination of characteristic building blocks, such as a tail group, molecular backbone, and headgroup. Among different kinds of SAMs, monolayers of thiols and disulfides on coinage metal substrates are probably the most frequently used ones because of their robustness, ease of preparation, and reasonable stability.[3,4] The thiolate headgroup emerging upon adsorption of thiols and disulfides provides sufficiently strong but flexible anchoring to the substrate, enabling efficient lateral diffusion of the adsorbed molecules to form highly ordered 2D assemblies. A noticeably stronger, covalent-like binding can result in the inhibition of the lateral mobility and poor structural perfection as it, for example, happens in siloxane-based SAMs on SiO_x, whereas a weaker anchoring is associated with a limited stability.[5]

Along with the strength of the headgroup–substrate bond, the corrugation of the binding energy surface for the given headgroup/substrate combination, that is, a two-dimensional energetic landscape of the substrate seen by the headgroups, is of importance.[1] In case of a strong corrugation, as occurs for thiolate-based SAMs on Au(111),[1,4,6−8] the molecular lattice becomes pinned to the structural template provided by the substrate, which can result in reduced packing density[1,4,6−8] and/or in limited structural perfection[9−13] if the optimal molecular arrangement does not fit the substrate structure. In contrast, a weak corrugation of the binding energy surface allows formation of optimal molecular lattices, mediated, to a significant extent, by the

* Address correspondence to michael.zharnikov@urz.uni-heidelberg.de, piotr.cyganik@uj.edu.pl, aterfort@chemie.uni-frankfurt.de.

Received for review February 17, 2015 and accepted April 10, 2015.

Published online April 10, 2015
10.1021/acsnano.5b01109

backbone−backbone interactions as this happens in alkanethiolate SAMs on Ag(111).[1,4,14,15] A further parameter associated with a particular headgroup−substrate combination is the bending potential which enters the balance of structural forces, affecting the packing density and molecular orientation.[16−19]

Apart from the structural effects, charge transport properties of molecular anchors are important because they define the electronic coupling of the SAM constituents to the (conductive) substrate. A good coupling is favorable for applications in molecular and organic electronics.[20,21] In the former case, this guarantees an efficient and rapid charge transfer between the functional molecule and the bottom electrode. In the latter case, this improves the conductivity of the buffer SAM film, improving the overall device performance. In addition, the docking chemistry at the substrate side of the SAM affects the level alignment at the metal−organic interface.[22]

In view of the above aspects, optimization of the headgroup seems to be a promising way to tune the structural and electronic properties of SAMs. Among other options, the use of elements with the same valence electron configurations as sulfur, such as its homologues in the 16th group of the periodic table, seems to be a reasonable choice for SAMs on coinage metal substrates. Accordingly, the suitable candidates are selenium and tellurium, with a clear preference for the former element in view of the limited stability of tellurium-based monolayers.[23] Along these lines, a variety of aliphatic and aromatic SAMs with the selenol headgroup have been prepared on Au(111) and Ag(111) substrates and studied to different extents.[19,24−45] The quality of these SAMs was in most cases comparable or even superior to that of the monolayers prepared from the thiol analogues. The latter was particularly the case for the aromatic SAMs on Au(111), including those with the phenyl, biphenyl, and anthracene backbone.[35,37,40−42,44] For these monolayers, a significant improvement of the quality in terms of the structural perfection, domain size, and long-range order was observed. This was explained by the ability of the selenolates to adjust the surface lattice of the substrate to the most favorable 2D arrangement of the SAM-building molecules[35,40,44] or, alternatively, by a smaller corrugation of the binding energy surface for selenolates on Au(111) as compared to that for thiolates.[37,41,40,44]

In spite of the general agreement regarding the quality improvement upon the use of selenium instead of sulfur as the headgroup, there is still a controversy regarding the strength of the headgroup−substrate bond for the thiol-based and selenol-based SAMs on Au(111). The selenium−gold bond was considered as both stronger[25,27,28,35,46] and weaker[24,37] than the sulfur−gold one. These controversial conclusions were derived on the basis of different experiments, using different test systems which were characterized to a limited extent only or/and were not equivalent. In particular, the conclusion regarding the comparably weaker selenium−gold bond was based on the results of thermal desorption spectroscopy experiments on benzenethiolate and benzeneselenolate SAMs which have rather different packing densities and quality.[37] A further controversial point is the conductance of the selenium−gold bond. According to some reports, thiolate-based molecules have a lower barrier to tunneling and therefore a higher conductance than their selenolate-based analogues.[47] At the same time, according to other reports, the electronic conductance of selenium-based aromatic molecules is comparable to that of their sulfur analogues.[22] Finally, there are several studies which claim that the charge injection barrier is lower for the gold−selenium bond than for the gold−sulfur bond,[48] and the electronic conductance of selenium-based molecules is significantly higher than that of their sulfur analogues.[49−51] The above discrepancies can be related to differences in the test systems used for the respective experimental studies and theoretical simulations (*e.g.*, aliphatic[47] or aromatic[49,50] ones) but also to certain limitations of the standard experimental approaches used to measure conductance in molecular assemblies. These limitations include an uncertainty regarding the number of molecules involved in the charge transport and quality of the top contact, that is, the electrical contact to the tail group of the molecules (the bottom contact is mediated by the headgroup and provided usually by the metal substrate).

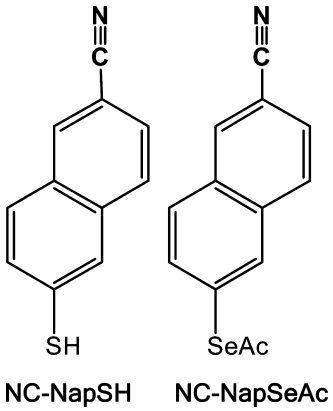

Figure 1. Molecules used in this study along with their acronyms. During the formation of the monolayers, the proton and the acetyl group, respectively, become cleaved off, so that the adsorbed molecules can be assigned as NC-NapS and NC-NapSe.

In the present work, we try to clarify the above-mentioned controversies using model systems based on 6-cyanonaphthalene-2-thiolate and -selenolate (NC-NapS and NC-NapSe, respectively; see Figure 1 for the starting materials) immobilized on Au(111) as SAMs. Both systems were characterized extensively by a combination of complementary spectroscopic and microscopic techniques, demonstrating the high

quality of the monolayers and providing a reliable basis for further dedicated experiments. Of particular importance were comparable packing densities and molecular orientations in both studied systems, which, in our opinion, are indispensable prerequisites for reliable comparison of these systems regarding bond strength and transport properties. The issue of the bond strength was addressed by exchange experiments and static secondary ion mass spectroscopy (S-SIMS). The question of the charge transport properties was pursued by resonant Auger electron spectroscopy (RAES) within the core−hole−clock (CHC) approach. This contact-free method allows monitoring of charge transfer (CT) dynamics on the femtosecond time scale following a resonant excitation of a core-level electron at a specific functional group to a bound state above the Fermi level of the substrate.[52−55] Such a dynamic is an important phenomenon on its own but is also a numerical fingerprint for the electrical transport properties of a particular molecule adsorbed on the solid support, relying on the inverse relation between the characteristic CT time and the current in a molecular junction. Significantly, the use of the CHC approach solves the problem of the top contact, along with the controversy regarding the amount of involved moieties since the results are representative of individual molecules. As a suitable functional group, serving as starting point of CT through the molecular framework to the substrate, the nitrile group (−C≡N) was utilized, following the positive experience of our previous studies.[56−59] This was the major reason to use nitrile-substituted naphthalenes instead of nonsubstituted ones. A further reason was a presumed positive impact of the nitrile group on the long-range order in the monolayers. According to the literature, the order in the SAMs of nonsubstituted naphthalene-2-thiol is either poor[60] or only local.[61,62] Finally, following a recently developed approach,[63,64] the nitrile group served as a suitable spectroscopic marker to unambiguously determine molecular orientation in the systems studied.

RESULTS AND DISCUSSION

General Comments. The NC-NapS and NC-NapSe films were prepared at room (RT) and elevated (60 °C) temperature. All experiments were performed on the samples prepared at 60 °C because of their superior quality, as will be shown in the next section. The structure and molecular organization in the films were studied by scanning tunneling microscopy (STM), high-resolution X-ray photoelectron spectroscopy (HRXPS), ellipsometry, infrared reflection absorption spectroscopy (IRRAS), and angle-resolved near-edge X-ray absorption fine structure (NEXAFS) spectroscopy. Specific questions were addressed by RAES, S-SIMS, and dedicated exchange experiments as described in the previous section.

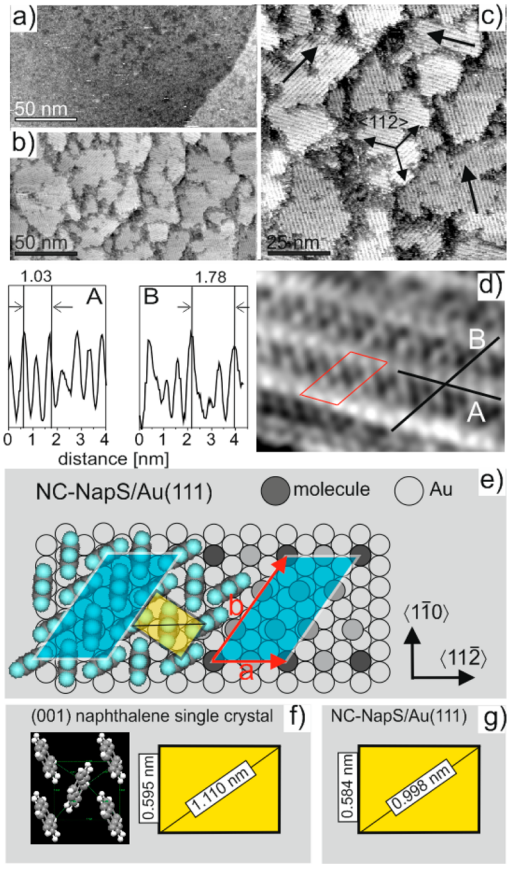

Figure 2. STM images taken with different resolutions for the NC-NapS SAMs on Au(111) prepared at room temperature (a) and at 60 °C (b−d). Height profiles A and B are taken along the lines depicted in (d); the profiles with the vertical scale included are presented in Figure S5a in the Supporting Information. The red box in (d) marks the oblique ($2\sqrt{3} \times \sqrt{37}$) unit cell schematically presented in (e). In (f), the 2D herringbone arrangement of the naphthalene molecules within the (001) plane of the naphthalene single crystal is shown, along with the respective rectangular unit cell (in yellow). A similar structural motif can be found in the STM images of the NC-NapS SAMs, as shown by the yellow rectangle in (e). The dimensions of this motif, as determined by STM, are presented in (g) for direct comparison with (f).

Scanning Tunneling Microscopy. Representative STM data obtained for the NC-NapS SAMs are presented in Figure 2. The images in Figure 2a,b, obtained from large areas, allow comparison of the overall morphology of the samples prepared at RT and 60 °C. In contrast to the rough and very defective surface observed for the sample prepared at RT (Figure 2a), the samples prepared at the elevated temperature show a distinct molecular structure with domains in the range of ∼20−40 nm (Figure 2b). At higher resolutions, these well-ordered domains exhibit a characteristic stripe pattern strictly following the ⟨11$\bar{2}$⟩ high-symmetry directions of the underlying Au(111) substrate (Figure 2c). The representative molecular resolution image shown in Figure 2d reveals that the NC-NapS SAMs form a high-density structure with a comparably large unit cell. The average dimensions of

this unit cell are $a = 1.03 \pm 0.04$ nm and $b = 1.78 \pm 0.05$ nm, as determined from the appropriate height profiles A and B in Figure 2d. Such a unit cell can be described as an oblique ($2\sqrt{3} \times \sqrt{37}$) structure, which is commensurate with the Au(111) substrate and has cell vectors of 1.00 and 1.75 nm length, respectively. With six molecules per unit cell, the molecular footprint for this structure amounts to 0.239 nm^2. A schematic cartoon with the possible herringbone arrangement of the NC-NapS molecules in this structure is shown in Figure 2e (for the sake of clarity, individual molecules are either presented as a phenyl ring or as a gray or black circle).

The above 2D arrangement can be compared with the crystal structure of the parent compound, naphthalene. It is well-known that naphthalene crystallizes in a monoclinic lattice with layered structure.[65] Figure 2f shows schematically the arrangement of molecules within the layers that correspond to the (001) planes. The naphthalene molecules adopt a herringbone structure with a rectangular unit cell (yellow rectangle), the shorter side of which is 0.595 nm, while its diagonal equals 1.11 nm. A similar rectangle can also be fitted into the motif of the oblique ($2\sqrt{3} \times \sqrt{37}$) structure shown in Figure 2e, with the dimensions of the shorter side and diagonal equal to 0.584 and 0.998 nm, respectively (see Figure 2g). This comparison proposes that the arrangement of NC-NapS molecules on the Au(111) surface within the ($2\sqrt{3} \times \sqrt{37}$) lattice has a certain similarity to the packing motif along the (001) plane in crystalline naphthalene.

A compilation of analogous STM data collected for the NC-NapSe monolayers on the Au(111) substrate is presented in Figure 3. As in the NC-NapS case, NC-NapSe SAMs prepared at RT are defective and unordered (Figure 3a), while the preparation at 60 °C results in extended ordered structures (Figure 3b). At higher resolution, these SAMs reveal well-defined domains, which, at first sight, have a similarly striped structure and similar dimensions (20−40 nm, Figure 3c) as those in the NC-NapS monolayers obtained as 60 °C (Figure 2c). However, in the NC-NapSe case, the stripes run along the $\langle 1\bar{1}0 \rangle$ high-symmetry directions of the Au(111) substrate, in contrast to the $\langle 11\bar{2} \rangle$ directions observed for the NC-NapS SAMs. A representative molecular resolution image shown in Figure 3d reveals that the NC-NapSe monolayers form a densely packed structure with a comparably small, rectangular unit cell. The average dimensions of this unit cell, $a = 0.61 \pm 0.03$ nm and $b = 0.75 \pm 0.05$ nm, marked in the characteristic cross sections A and B in Figure 3d, are very close to the rectangular ($2 \times 1.5\sqrt{3}$) structure of the nonreconstructed substrate, with cell dimensions of 0.58 nm × 0.75 nm, corresponding to a molecular footprint of 0.215 nm^2 (~11% less than the value for NC-NapS/Au). Thus, presumably, the structure of the NC-NapSe monolayer mimics that of the

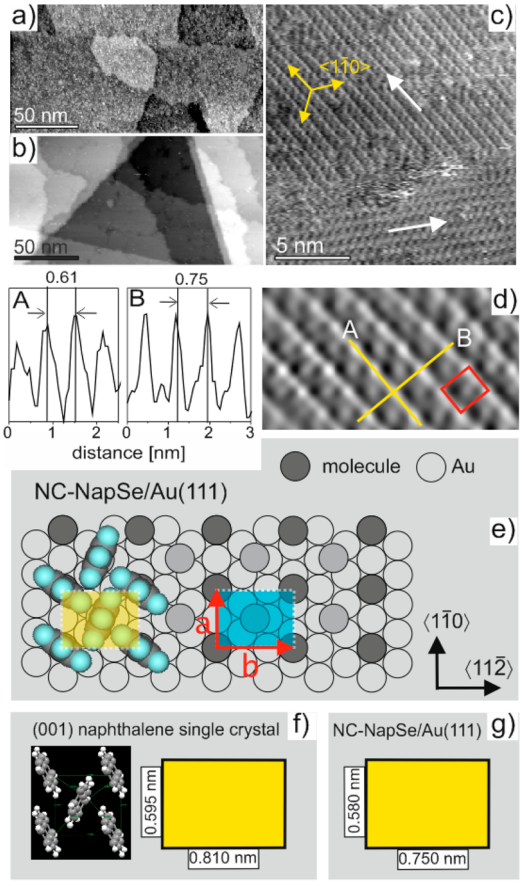

Figure 3. STM images taken with different resolutions for the NC-NapSe SAMs on Au(111) prepared at room temperature (a) and at 60 °C (b−d). Height profiles A and B are taken along the lines depicted in (d); the profiles with the vertical scale included are presented in Figure S5b in the Supporting Information. The red box in (d) marks the rectangular ($2 \times 1.5\sqrt{3}$) unit cell schematically presented in (e). In (f), 2D herringbone arrangement of naphthalene molecules within the (001) plane of the naphthalene single crystal is shown, along with the respective rectangular unit cell (in yellow). A similar structural motif can be found in the STM images of the NC-NapSe SAMs, as shown by the yellow rectangle in (e). The dimensions of this motif, as determined by STM, are presented in (g) for direct comparison with (f).

nonreconstructed substrate, even though the basic ($2 \times 1.5\sqrt{3}$)*rect* unit cell is incommensurate with the substrate. As commensurate entity, a double unit cell, a ($2 \times 3\sqrt{3}$)*rect* structure, can be considered strictly within the Wood's notation. Regardless of this formality, the observed packing motif is simple and has a strong similarity to the molecular arrangement within the (001) plane of crystalline naphthalene, as shown in the cartoons in Figure 3f,g.

High-Resolution X-ray Photoelectron Spectroscopy. C 1s, N 1s, S 2p, and Se 3d HRXP spectra of the NC-NapS and NC-NapSe films prepared at 60 °C are presented in Figure 4. They go in line with the formation of well-defined SAMs. Indeed, the S 2p spectrum of NC-NapS/Au in Figure 4d exhibits a distinct S $2p_{3/2,1/2}$ doublet at a binding energy (BE) position of ~162.0 eV (S $2p_{3/2}$) with no traces of atomic sulfur, disulfide, unbound

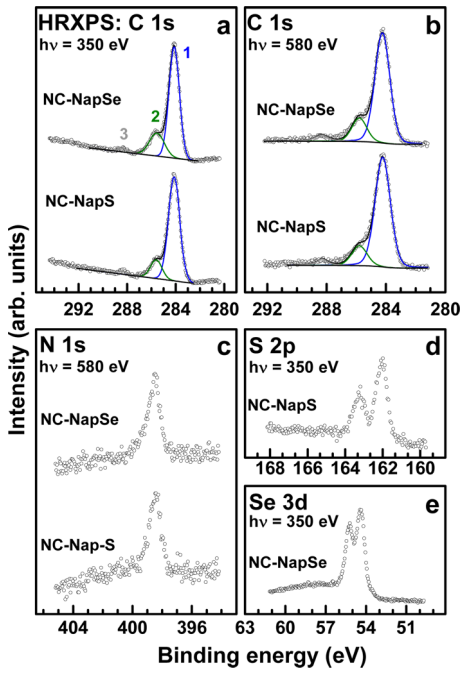

Figure 4. C 1s (a,b), N 1s (c), S 2p (d), and Se 3d (e) HRXP spectra of the NC-NapS and NC-NapSe SAMs. The C 1s spectra are decomposed in individual emissions, *viz*. main peak (1; blue line), high BE shoulder (2; olive line), and a low-intensity feature (3; gray line). The photon energies are given in the panels.

thiol, or oxidized species. This BE value corresponds to the thiolate species bound to noble metal surfaces,[66−68] which suggests that basically all molecules in the NC-NapS films were anchored to the substrate *via* a thiolate−gold bond, as should be the case for well-defined SAMs. Similarly, the Se 3d spectrum of NC-NapSe/Au in Figure 4e exhibits a sole Se $3d_{5/2,3/2}$ doublet at a BE position of ∼54.25 eV (Se $3d_{5/2}$) characteristic of the selenolate species bound to noble metal surfaces.[34,35,39,68] This means that basically all molecules in the NC-NapSe films were anchored to the substrate *via* a selenolate−gold bond, forming well-defined SAMs.

The C 1s spectra of the NC-NapS and NC-NapSe monolayers in Figure 4a,b exhibit an intense emission at a BE of 284.15 eV (**1**) accompanied by a weak shoulder at higher BE (285.65 eV) (**2**). The intense emission can be assigned to the naphthalene backbone, while the high BE shoulder can be mainly associated with the nitrile carbon, similar to the case of nitrile-substituted oligophenylenes and oligo(phenylene ethynylene)s.[64,69] In accordance with the above assignment, the relative intensity of the shoulder decreases with increasing photon energy as follows from comparison of Figure 4a,b. This happens because the larger inelastic mean free path at higher kinetic electron energies favors photoemission from the backbone (inner part of the sample) compared to that from the tail group (outer surface of the sample). This decrease is stronger for NC-NapSe/Au than for NC-NapS/Au, which is presumably related to an admixture of a weak signal from a minor contamination (CO) to the shoulder, with a somewhat higher contribution for NC-NapS/Au. In addition, there is a low-intensity feature at 288.3 eV (**3**), related presumably to another minor contamination such as COOH. The contamination was most likely located at the SAM−substrate interface since its relative weight increased with increasing kinetic energy of the photoelectrons.

The N 1s spectra of the NC-NapS and NC-NapSe SAMs in Figure 4c exhibit a single N 1s emission at a BE of 398.5 eV. This emission can be assigned to the nitrogen atom of the nitrile group, similar to the analogous systems.[58,64,69] The presence of the single emission only suggests the same chemical state and location within the SAMs for all nitrile groups. In view of the given attachment geometry (see the discussion regarding the S 2p and Se 3d HRXP spectra), all nitrile groups are exclusively located at the SAM−ambience interface.

Apart from the above analysis of the HRXP spectra, characteristic intensity relations were considered. In particular, the C 1s/Au 4f intensity ratio for the NC-NapSe SAMs was found to be slightly higher than that for the NC-NapS monolayers at both excitation energies used (350 and 580 eV). Accordingly, the effective thickness of the former films (∼1.17 nm), calculated within the standard approach,[70,71] was found to be slightly (by ∼11%) larger than that of the latter films (∼1.05 nm). This suggests a slightly higher packing density of the NC-NapSe SAMs as compared to the NC-NapS monolayers, in full agreement with the STM data which give a similar difference in the molecular footprint between NC-NapSe/Au and NC-NapS/Au. Significantly, the thickness values are very close to the lengths of the NapS and NC-NapSe precursors (1.12 and 1.14 nm, respectively), implying dense molecular packing in the monolayers, once more, in agreement with the STM data.

Ellipsometry and Infrared Reflection Absorption Spectroscopy. The HRXPS results were verified by ellipsometry. Accordingly, the thicknesses of the NC-NapS and NC-NapSe films were estimated at 1.03 ± 0.08 and 1.19 ± 0.04 nm, respectively. These values agree well with the effective thicknesses derived on the basis of the HRXPS data, corroborating the reliability of the results.

The films were further characterized by IRRAS. In Figure 5, experimental and calculated spectra of the NC-NapS and NC-NapSe species and the respective SAMs are compiled. The assignment of the bands to certain vibrational modes (see Table S1 in the Supporting Information) was performed with the help of calculated spectra of isolated nitrile-substituted naphthalenethiol and -selenoacetate molecules. The IRRA spectra of the NC-NapS and NC-NapSe films confirm formation of well-defined monolayers. In particular, for the NC-NapSe film, the absence of bands related to the acetate moiety (**2** and **5**) indicates that this group has been

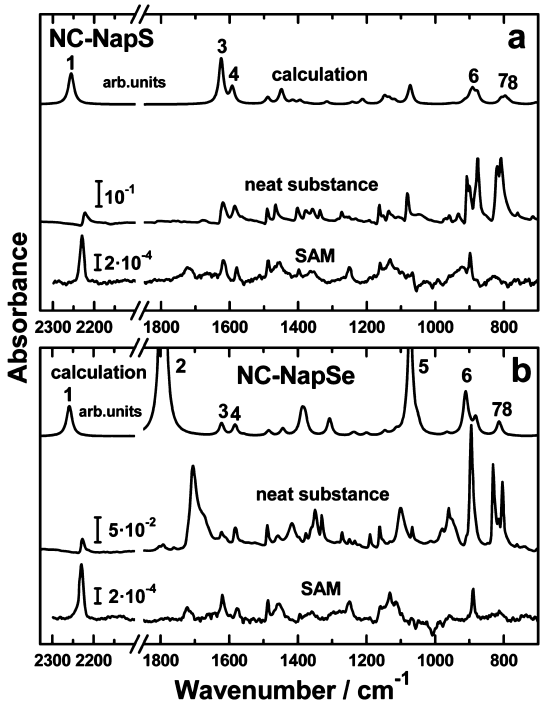

Figure 5. IR spectra for NC-NapSH/NC-NapS (a) and NC-NapSeAc/NC-NapSe (b). The upper traces represent calculated spectra of the isolated molecules using DFT; the middle traces show the spectra of the neat substances (NC-NapSH and NC-NapSeAc); in the lower traces, the IRRA spectra of the NC-NapS and NC-NapSe SAMs on Au are displayed. The theoretical spectra are scaled in arbitrary units; the scale bars for the absorbance of the experimental spectra are given in the figure. The most important vibrational bands are designated with numbers. See text for details.

cleaved off upon the formation of a gold−selenolate bond, as has been expected.[41] Significantly, for both NC-NapS and NC-NapSe films, bands with out-of-plane transition dipole moments (TDMs; **7** and **8**) are clearly attenuated in comparison to bands with TDMs parallel to the C≡N bond axis (**1**, **3**, **4**, **6**). In view of the surface selection rule for metal substrates,[72] this behavior leads to the assumption that the aromatic backbones of the NC-NapS and NC-NapSe molecules are oriented predominantly perpendicular to the substrate surface, corresponding to the entire upright orientation of the SAM constituents.

Note that the intensities of the C≡N stretch bands (**1**) in the IRRA spectra of NC-NapSe/Au are slightly larger than that in the spectra of NC-NapS/Au. This can be caused either by a somewhat more upright orientation of the NC-NapSe molecules or by a higher surface coverage, which is presumably the case in view of the STM, HRXPS, and ellipsometry data. As for the exact molecular orientation, it could be better addressed by NEXAFS spectroscopy, as will be described in the next section.

Near-Edge X-ray Absorption Fine Structure Spectroscopy. The C K-edge NEXAFS spectra of the NC-NapS and NC-NapSe SAMs are presented in Figure 6a. This figure compiles the spectra acquired at an X-ray incidence angle of 55° as well as the difference between the spectra acquired at X-ray incidence angles of 90 and 20°. The angle of 55° is the so-called magic angle of X-ray incidence; at this orientation, the spectrum is not affected by any effects related to molecular orientation and is therefore exclusively representative of the chemical identity of investigated samples.[73] In contrast, the difference of the NEXAFS spectra acquired at normal (90°) and grazing (20°) angles of X-ray incidence is a fingerprint of the linear dichroism and, thus, representative of the molecular orientation and orientational order in the system studied.

The spectra in Figure 6a exhibit a variety of overlapping absorption resonances in the pre-edge area and in the vicinity of the absorption edge. To distinguish between individual resonances, this region is presented separately in Figure 6b, along with the spectra of two reference systems, that is, SAMs of nonsubstituted naphthalene-2-thiol (NapS) and nitrile-substituted biphenylthiol (NC-BPT)[63,64] on Au(111). The spectrum of the NC-BPT film exhibits typical features of poly-*p*-phenylenes,[73−76] π_1* (**1**), π_2* (**2**), and σ_1* (**3**) resonances of the phenyl rings at 285.0, 288.5, and 292.9 eV, respectively, along with the double π* resonance at 286.0 and 286.7 eV (**4** and **5**) associated with the terminal benzonitrile moiety.[58,64,69] The dominant π_1* resonance splits into two contributions (**1a** and **1b**), at 284.65 and 285.4 eV, when passing from the NC-BPT to NapS monolayer. Such a splitting is typical for acenes[75,77−80] and is explained by the chemical shift of the two symmetry-independent carbon atoms.[78] Apart from this splitting and the lack of the benzonitrile-related resonances (**4** and **5**), the spectrum of the NapS film mimics that of the NC-BPT SAM, exhibiting the same resonances (**2** and **3**), along with a R*/C−S* resonance at 286.8 eV. In accordance with the molecular structure, the spectra of the NC-NapS and NC-NapSe SAMs exhibit resonances characteristic of both nonsubstituted naphthalene (**1a**, **1b**, **2**, and **3**) and benzonitrile (**4** and **5**). Distinct differences are a renormalization of the relative intensities of the **1a** and **1b** resonances and an increase in the relative intensity of the major benzonitrile-related feature (**5**). These changes can be tentatively explained by the conjugation between the π* systems of the nitrile moiety and naphthalene backbone, resulting in a redistribution of the electron density and, subsequently, in changes in the oscillator strengths of the involved electronic transitions.

The N K-edge NEXAFS spectra of the NC-NapS and NC-NapSe SAMs are presented in Figure 6c. These spectra are dominated by a double π* resonance at ~398.8 and ~399.7 eV, accompanied by a weak feature at ~401.7 eV (presumably π_4* of nitrile)[81,82] and several hardly perceptible σ* resonances at higher PEs. The double π* resonance is characteristic of benzonitrile and observed for the gas phase,[82] molecular solid,[81] and monomolecular films containing this moiety.[58,64,69]

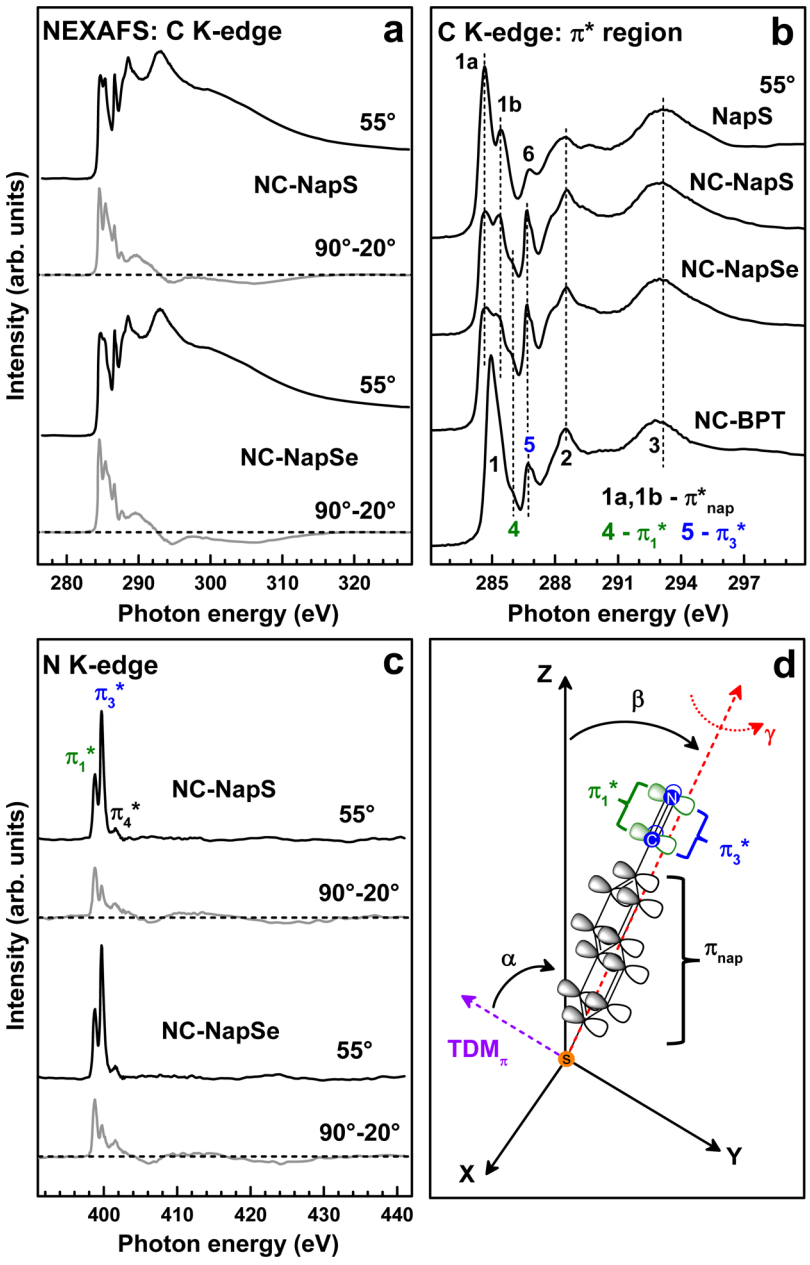

Figure 6. C (a,b) and N (c) K-edge NEXAFS spectra of the NC-NapS and NC-NapSe SAMs acquired at an X-ray incident angle of 55° (black solid curves), along with the respective difference between the spectra collected under normal (90°) and grazing (20°) incidence geometry (gray solid curves in a and c). The horizontal dashed lines correspond to zero. In (b), the region of the π^* resonances is presented, and the spectra of several reference systems such as NapS and NC-BPT SAMs are given for comparison. Individual resonances in b and c are marked, in b by numbers; see text for details. The vertical dashed lines are guides for the eye. (d) Schematic drawing of the orientation of the NC-NapS and NC-NapSe molecules in the respective SAMs. The π_{nap}* orbitals of the naphthalene backbone (black) and the π_1* orbital of the nitrile group (green) are parallel to each other and perpendicular to the molecular plane; the respective transition dipole moment TDM_π is shown as a violet arrow; its orientation is given by the angle α. The π_3* orbital of the nitrile group (blue) is parallel to the molecular plane. The backbone tilt angle β and twist angle γ describe the molecular orientation. At γ = 0, TDM_π lies in the plane spanned by the *z*- and the molecular axis (red dashed line). Black, green, and blue are used to color-code the respective resonances in b and c.

The appearance of this resonance is related to the conjugation between the π^* orbitals of the nitrile group and the adjacent phenyl ring. As a result, the degeneration of the π(C≡N*) orbital is lifted and it splits into two orbitals with distinctly different energies (in contrast to nitrile-substituted alkanethiols where the energies are quite close),[56,57,59] which are oriented either perpendicular (lower PE; π_1*) or parallel (higher PE; π_3*) to the plane of the adjacent ring,[81,82] as schematically shown in Figure 6d. The comparably lower intensity of the π_1* resonance can be explained by the delocalization of the respective orbital over the entire benzonitrile moiety, whereas π_3* is exclusively localized at the nitrile group.

TABLE 1. Average Tilt Angles of the π_{nap}* (1 and 2) and $\pi_{1,3}$*(NC) Orbitals Derived from the Numerical Evaluation of the NEXAFS Data for the NC-NapS, NC-NapSe, and NapS SAMs and the Average Molecular Tilt and Twist Angles of the Molecular Backbone (Error Bars Can Be Estimated at ±3°)

average angles/system	NC-NapS	NC-NapSe	NapS
π* orbitals (naphthalene) − α_{nap}	68°	67°	71°
π_1* orbital (NC) − α_1	66°	67°	
π_3* orbital (NC) − α_3	57°	57°	
twist angle (γ) from α_1 and α_3	52°	54°	
molecular tilt (β) from α_1 and α_3	43°	42°	
molecular tilt (β) from α_{nap} and $\gamma(\alpha_1,\alpha_3)$	38°	41°	

The C and N K-edge NEXAFS spectra of NC-NapS and NC-NapSe SAMs exhibit pronounced linear dichroism as follows from the respective difference curves in Figure 6a,c. Considering that the TDMs associated with the dominant π* resonances are oriented perpendicular to the molecular axis, the positive sign of the respective difference peaks suggests an upright orientation of the molecules in the SAMs. This qualitative conclusion goes in line with the one drawn from the IR spectra of these films (see above). While a quantitative evaluation of the IR data was not possible, the entire set of NEXAFS spectra could be processed self-consistently to obtain exact twist and tilt angles. Within this procedure, performed within the standard theoretical framework for vector type molecular orbitals,[73,76] the average tilt angles of the most dominant π* orbitals of the naphthalene backbone (**1a** and **1b**, see Figure 6b) and the nitrile moiety (π_1* and π_3*, see Figure 6c) were derived. They are compiled in Table 1, along with the analogous value for the reference NapS SAMs. A schematic drawing of the target molecules, along with the relevant molecular orbitals and angles, is presented in Figure 6d.

Based on the derived angle values for the NC-NapS and NC-NapSe SAMs, average tilt and twist angles for the molecular backbones in these monolayers were determined with the following equations

$$\cos(\alpha_1) = \sin(\beta)\cos(\gamma) \quad (1)$$

$$\cos(\alpha_3) = \sin(\beta)\cos(\pi/2 - \gamma) \quad (2)$$

and

$$\cos(\alpha_{nap}) = \sin(\beta)\cos(\gamma) \quad (3)$$

within the established evaluation procedure.[63,64,69] Note that the determination of both tilt and twist of the naphthalene backbones in the target SAMs was only possible due to the attachment of the nitrile tail groups to these backbones and alignment of the orthogonal π_1* and π_3* orbitals of this groups with the π_{nap}* orbitals. Without this dedicated tail group, only the average orientation of the TDM$_{\pi^*}$ can be determined. The molecular tilt can then only be evaluated within an assumption regarding the value of the twist angle. Such an assumption, even though reasonable (*e.g.*, based on the data for the respective bulk systems or indirect data by other techniques),[17] is of course inferior to the direct determination of the twist angle, as in the present case.

The derived tilt and twist values for NC-NapS and NC-NapSe SAMs are compiled in Table 1. Significantly, the tilt angles calculated from the system of eqs 1 and 2 are very close to the analogous values calculated from eq 3. This underlines the reliability of the approach—in view of the fact that the above calculations were based on the independently determined values for the different building blocks of the target molecules, that is, the naphthalene backbone and nitrile group. According to Table 1, the average tilt and twist angles of the molecular backbones in the NC-NapS and NC-NapSe SAMs are very similar, being ~41 and ~53°, respectively. Note that the values of the tilt angles are in accordance with the attenuation of the out-of-plane bands in the IRRA spectra of the SAMs (see above).

The relatively high tilt can be a consequence of the dipole−dipole interaction between the nitrile tail groups at the SAM−ambience interface. Minimization of this unfavorable interaction can be achieved by the tilting of the nitrile groups,[83,84] along with the rigidly bound naphthalene backbones. Note that the nonsymmetrical attachment of these backbones to the thiolate and selenolate headgroups provides an additional rotational degree of freedom for the naphthalene unit,[62] similar to the case of anthracene-substituted alkanethiolates.[80] This permits an easy adoption of the most suitable orientation of the molecular backbones, depending on the balance of the structure−building interactions.

In agreement with the above hypothesis, the average tilt angle of the π* orbital in the NapS monolayers is larger than those in the NC-NapS and NC-NapSe SAMs (see Table 1). This suggests a smaller molecular inclination, even at the same twist angle as for the nitrile-substituted films. At a lower twist angle, such as for the respective bulk material (25°), the molecular inclination is even smaller, being 22°, which is very close to the analogous value for the bulk naphthalene (20.5°).

Exchange Experiments. To compare the relative stability of the S−Au(111) and Se−Au(111) bonds, exchange experiments were performed by incubation of the NC-NapS or NC-NapSe SAMs formed at 60 °C in ethanolic solution of hexadecanethiol (HDT) (see Methods for details). The progress of the exchange reaction was monitored by the advancing water contact angle (WCA) goniometry. The respective data obtained for the NC-NapS and NC-NapSe monolayers are summarized in Figure 7a. The WCA values for the freshly prepared films (*i.e.*, at an incubation time of 0 h) are identical (~50°) within the measurements precision and characteristic of hydrophilic surfaces, as can be expected.

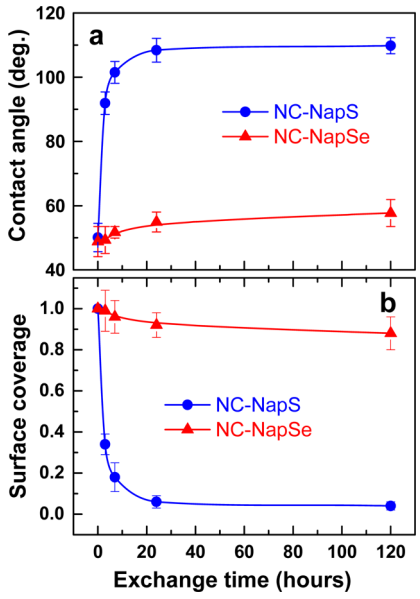

Figure 7. WCA (a) and relative surface coverage of the NC-NapS(Se) molecules (b) derived in the course of the exchange reaction between the NC-NapS (blue) or NC-NapSe (red) SAMs on Au(111) and HDT molecules in solution. The lines are guides for the eyes. See text for details.

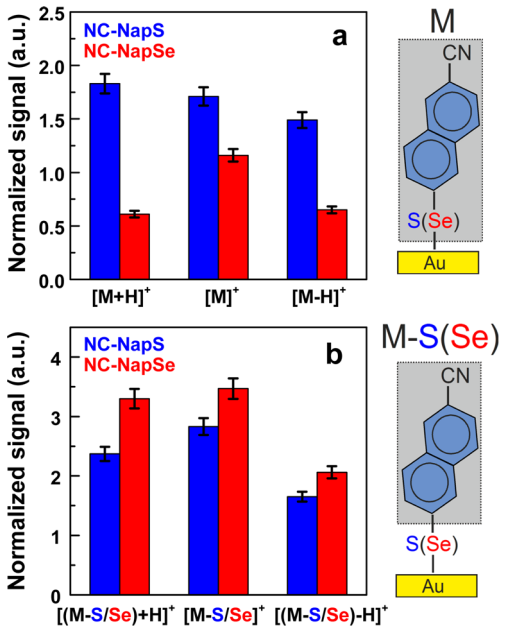

Figure 8. S-SIMS data analysis. (a) Normalized signal of the $[M + H]^+$, $[M]^+$, and $[M - H]^+$ secondary ions related to the desorption of the complete molecules for NC-NapS/Au(111) (blue bars) and NC-NapSe/Au(111) (red bars) SAMs. (b) Analogous data for the secondary ions related to the desorption of desulfurized fragments from NC-NapS/Au(111), *viz.* $[(M - S) + H]^+$, $[M - S]^+$, and $[(M - S) - H]^+$ (red bars) as well as deselenized fragments from NC-NapSe/Au(111), *viz.* $[(M - Se) + H]^+$, $[M - Se]^+$, and $[(M - Se) - H]^+$ (blue bars).

The analysis of the WCA values as functions of the incubation time in the HDT solution shows drastic differences between the NC-NapS and NC-NapSe SAMs. Whereas, in the former case, WCA is gradually changing from its initial value of 50° toward the value of about 110°, which is very close to the WCA measured for freshly prepared HDT/Au(111) (112°), only a small change (to ~55°) is observed for the selenolate SAM. The respective change in the molecular composition as a function of the incubation time in the HDT solution was calculated on the basis of the Cassie law[85]

$$\cos\theta_C = f_A\cos\theta_A + f_B\cos\theta_B;\ f_A + f_B = 1 \qquad (4)$$

which describes the effective contact angle value θ_C for a surface covered by fractions f_A and f_B of the materials A and B, the neat surfaces of which would expose contact angle values of θ_A and θ_B, respectively. The result of the calculations, based on the data shown in Figure 7a, is presented in Figure 7b. As shown in this figure, there is a nearly complete (~95%) exchange reaction between the HDT molecules in solution and the NC-NapS moieties on Au(111). In contrast, an analogous analysis for the NC-NapSe SAMs yields an extent of exchange of only ~10% during the entire reaction time (120 h). This suggests that only the defect sites in the original film were involved before the reaction was apparently terminated, presumably due to the high stability of the densely packed selenolate–SAM structure.

Secondary Ion Mass Spectrometry. Another technique, which recently proved to be extremely powerful for the determination of relative stabilities of headgroup–substrate bonds, is static SIMS (S-SIMS).[86] As documented in Figure S6 in the Supporting Information, both negative and positive ion mass spectra of the NC-NapS and the NC-NapSe SAMs were recorded. These spectra exhibit secondary ion signals typical of SAMs on gold, that is, sulfur(selenium)–gold clusters (having the general form of $[Au_xS(Se)_y]^-$), different molecular fragments, and metal–molecule clusters. To gain information related to the molecule–substrate interface stability, we have focused on analyzing in detail the signals of the positive ions associated with the complete molecules ($[M]^+$ = $[NC\text{-}NapS(Se)]^+$) and the desulfurized (or deselenized) fragments ($[M - S(Se)]^+$ = $[NC\text{-}Nap]^+$) emitted as a result of the ion-impact-induced breaking of the Au–S(Se) and S(Se)–C bonds, respectively (see the schematic cartoon in Figure 8). The relative intensities of these particular ions as well as of the related ions resulting from removing or attaching a single H atom are presented in Figure 8. The comparison of these data shows that, whereas the ion-induced desorption of the complete molecule is much more efficient for the NC-NapS as compared to the NC-NapSe SAMs, the opposite relation occurs for the desorption of the desulfurized and deselenized fragments, with a noticeably lower extent in the NC-NapS case.

Resonant Auger Electron Spectroscopy. As mentioned in the introduction, the issue of electronic conductance in the NC-NapS and NC-NapSe SAMs was tested by RAES

at the N K-edge within the CHC approach. As shown by the HRXPS and NEXAFS data, the nitrile groups were exclusively located at the SAM−ambience interface, being electronically connected to the substrate through the molecular framework. Thus, the CT pathway to the substrate at the resonant excitation of the nitrile group was well-defined. However, such a CT could only occur if it is energetically allowed. For efficient electron transport, the energy of the π^* resonantly excited electron at the nitrile group should be positive with respect to the Fermi level of the substrate. Accordingly, the π^* resonance excitation energy should be higher than the BE of the respective core electron. Luckily, in the case of the NC-NapS and NC-NapSe SAMs, this condition is well fulfilled for both π_1^* and π_3^* orbitals, the excitation energies of which (~399.7 and ~398.8 eV, respectively) are higher than that of the N 1s BE (398.5 eV). Thus, tail group-to-substrate transfer of the resonantly excited electron is energetically allowed for both [N 1s]π_1^* and [N 1s]π_3^* excitations.

As shown and described in Figure 9a, the decay of these excitations can occur in three possible ways if radiative decay is neglected. These include, first and foremost, so-called participator (P) and spectator (SP) scenarios, resulting in final states with either one hole in the region of the occupied valence (OV) states, corresponding to the P process, or two holes in the OV states but an additional electron in the unoccupied valence (UV) states, which gives in integral one hole per excited atom and corresponds to the SP process. Additionally, CT of the excited electron to the conduction band (CB) of the substrate can occur, followed by the standard Auger decay. This route leads to the final state with two holes in OV, which is nearly identical to the final state of the Auger decay in the case of nonresonant excitation, apart from subtle effects like alignment of the core hole or difference in vibrational fine structure.[87] Since all above final states are different, also in the terms of charge, the features related to the respective scenarios can be distinguished in the joint RAE spectrum as far as the target group is clearly defined and the resonant excitation does not interfere too much with the contributions from other processes (*e.g.*, photoemission) or other functional groups within the molecule.

An important point is that, generally, one cannot distinguish between CT to the substrate, through the molecular backbone, and CT to the backbone only in the CHC experiments involving a resonantly excitable tail group. Indeed, in both cases, the excited electron is not located any more at the terminal nitrile group, leading to the electronic configuration, which is nearly identical to the final state of the Auger decay in the case of nonresonant excitation. However, for CT to the backbone only, no dependence on the length of the backbone can be expected, which is not the case for both aliphatic and aromatic SAMs with the nitrile substitution.[57,58] This suggests that we indeed deal with the CT to the substrate, supported also by the energetic considerations (see above).

[N 1s]π_1^* and [N 1s]π_3^* RAE spectra of the NC-NapS and NC-NapSe SAMs along with their reproductions by the linear combination of the purely resonant (P and SP) and nonresonant (CT) contributions are presented in Figure 9b,c, respectively. The purely resonant contributions were measured using a reference nitrile-substituted terphenylthiol (NC-TPT) monolayer on Au(111). This molecule has the same benzonitrile functional group as the NC-NapS and NC-NapSe moieties but is too long to have a perceptible CT contribution in the RAE spectrum.[58] The RAE spectra of the NC-NapS and NC-NapSe SAMs exhibit both participator and spectator contributions, with a very low spectral weight of the former component in the [N 1s]π_3^* case. These spectra are very similar to the analogous spectra of other benzonitrile-terminated monomolecular films, which were analyzed in detail elsewhere.[58,64,69]

Analysis of the [N 1s]π_1^* RAE spectra in Figure 9b suggests that they contain considerable contributions from the CT route, represented as an admixture of the nonresonant spectrum to the pure resonant curves. Reconstruction of the RAE spectra by a linear combination of the nonresonant and pure resonant line shapes reproduces the experimental curves quite fairly, giving the identical portions of the nonresonant features (~21%), representative of CT, for both the NC-NapS and NC-NapSe SAMs. Based on these values, we can apply the main formula of the CHC approach, $\tau_{CT} = \tau_{core}(1 - P_{CT})/P_{CT}$, where τ_{core} is the known lifetime of inner shell vacancy (6.4 fs for N 1s)[88] and P_{CT} is the relative intensity of the post-CT portion in the total decay spectrum.[52−55,89] Accordingly, the derived τ_{CT} for both NC-NapS and NC-NapSe SAMs is 24 ± 4 fs. As expected, this characteristic time is longer than the analogous value for the monolayers of nitrile-substituted phenylthiolates (NC-PT; 9 ± 3 fs)[58] but smaller than the value for the SAMs of NC-BPT (29 ± 6 fs).[58] Most important is the fact that τ_{CT} is practically identical for the NC-NapS and NC-NapSe SAMs, differing by either thiolate or selenolate binding to the substrate.

In contrast to the [N 1s]π_1^* data, the [N 1s]π_3^* RAE spectra of the NC-NapS and NC-NapSe SAMs, presented in Figure 9c, do not exhibit any perceptible admixture of the nonresonant line shape. These spectra are practically identical to the properly scaled pure resonant spectra. Presumably, the characteristic CT time following the [N 1s]π_3^* excitation in the NC-NapS and NC-NapSe SAMs is much longer (more than 120−150 fs) than the N 1s core hole lifetime and is therefore not resolvable within the applied CHC scheme. Note that the analogous situation occurs for the NC-BPT SAMs, as well, and, consequently, is understandable in the case of the naphthalene backbone. Note also that the distinctly different τ_{CT} for the

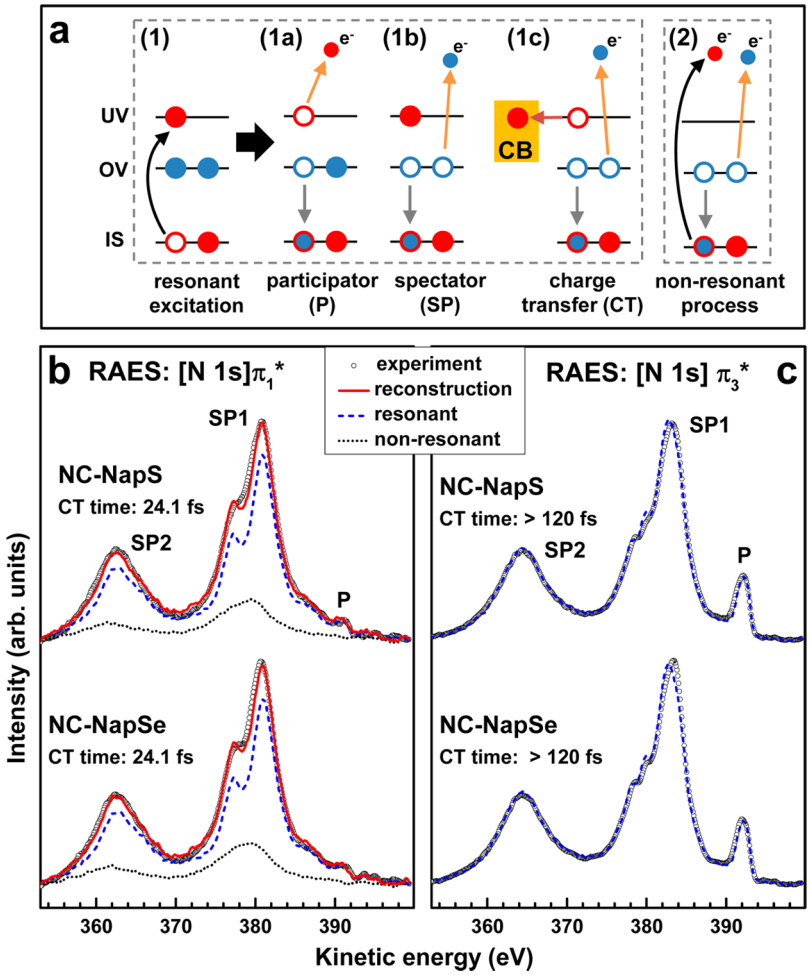

Figure 9. (a) Scheme of core excitation/de-excitation routes for the nitrile group in the NC-NapS and NC-NapSe SAMs in the framework of RAES (1). This group is considered to be weakly coupled to a continuum (*e.g.*, substrate conduction band, CB), with IS, OV, and UV denoting inner shell (here N 1s) and occupied and unoccupied 2s- and 2p-derived valence levels, respectively. Filled and hollow circles represent electrons and holes, respectively, with red and blue color-code corresponding to IS and OV/UV, respectively. Shallow core holes as the N 1s decay nearly exclusively by an Auger process; that is, an electron from OV fills the hole (gray arrow), and a second electron carrying the excess energy is emitted (orange arrow). Upon the resonant excitation of an IS electron (black arrow in 1) into a bound state (UV), the excited electron can either take part in this decay process (participator, P) or "watch" it as a spectator (SP). Both P and SP processes lead to characteristic final states with effectively one hole in the valence region. Alternatively, CT of the excited electron to CB can occur (brown arrow), leading to the same final state with two holes in OV as the nonresonant Auger process (2), such as the excitation of an IS electron into a continuum state (black arrow in 2) followed by the emission of an OV electron. [N 1s]π_1* (b) and [N 1s]π_3* (c) RAE spectra of the NC-NapS and NC-NapSe SAMs (open circles) along with their reproductions (red solid lines in b) by the linear combination of the purely resonant (blue dashed lines) and nonresonant (black dotted lines in b) contributions. P and SP features are marked. The derived τ_{CT} values are given. The experimental and resonant spectra are almost identical in c, so that the nonresonant contribution is too small to be perceptible.

[N 1s]π_1* and [N 1s]π_3* excitations are a common phenomenon in benzonitrile-substituted monolayers.[58] This difference was explained by the different conjugations of the relevant molecular orbitals.[58] As mentioned above, the π_1* orbital is strongly conjugated with the π* system of the adjacent phenyl ring, which makes the electron transport along the molecular backbone more efficient. In contrast, the π_3* orbital is almost exclusively located at the nitrile group, which can be associated with a longer CT pathway and an additional injection barrier.

DISCUSSION

We start the discussion with a summary of the basic characterization data for both systems studied, which is a critical step to give credibility to the stability and CT dynamics experiments. When looking at the effect of the S→Se headgroup substitution on the stability and transport properties of SAMs, it is not sufficient to use just the S- and Se-based molecular analogues, as it is fulfilled in a variety of previous publications[37,41,47,51] and also in the present case, but it needs also to be ensured that the respective SAMs formed by these analogues have similar structure and packing density, so that the relative stability and conductance data can be exclusively related to the SAM–Au(111) interface modification.

In the framework of these basic requirements, our STM analysis demonstrates that the NC-NapS and

NC-NapSe SAMs prepared on Au(111) at slightly elevated solution temperature (60 °C) exhibit well-ordered oblique ($2\sqrt{3} \times \sqrt{37}$) and rectangular ($2 \times 1.5\sqrt{3}$) molecular arrangements, respectively. Importantly, both structures are characterized by similar (within ~10%) packing densities. These conclusions, based on the "local" STM analysis, are fully consistent with the results obtained by "large area" techniques, such as ellipsometry, IRRAS, XPS, and NEXAFS spectroscopy, which show similar effective film thicknesses (~10.5 and ~11.7 Å) as well as basically identical average tilt (~41°) and twist (~53°) angles of the molecular backbones for the both types of SAMs. Such consistency of the data obtained from the local and global techniques is crucial at this point because all further analysis of the stability and transport properties of these SAMs is based on the global techniques which sample a large area, averaging over possible structural defects.

Despite similar packing densities, the STM analysis of the NC-NapS and NC-NapSe SAMs on Au(111) also shows important structural differences. It can be assumed that, in analogy to similar systems,[41] the molecules in these SAMs adopt a structure which mimics the characteristic herringbone arrangement known for crystalline naphthalene. For the NC-NapSe SAM, a simple rectangular ($2 \times 1.5\sqrt{3}$) unit cell, involving three different adsorption sites, was observed (see Figure 3e), which, within the precision of our STM measurements, corresponds directly to the molecular arrangement within the (001) plane of crystalline naphthalene. Formation of such a simple structure, close to that of crystalline naphthalene, implies that the NC-NapSe molecules are capable of achieving an optimal, single-crystal-like molecular arrangement even at the comparatively stronger interaction with the substrate. A distinctly different situation occurs in the case of the NC-NapS SAMs. Here, a somewhat larger, oblique ($2\sqrt{3} \times \sqrt{37}$) unit cell is observed, which is fully commensurate with the Au(111) substrate but is much more complex, exhibiting up to six different adsorption sites. As indicated in Figure 2e, it is still possible to fit the motif found within the (001) plane of crystalline naphthalene into the oblique ($2\sqrt{3} \times \sqrt{37}$) cell but only relying on the average distances between the molecules inside this complex structure. These observations indicate that the intermolecular interactions in the NC-NapS SAMs are inferior to the molecule–substrate interface energetics, so that the structural template provided by the substrate is a dominant factor for the structure formation. Significantly, since the packing motive and the density for both types of SAMs are very similar, we can assume that the observed difference in balancing the impact of the intermolecular interactions and molecule–substrate interface energetics on the 2D structure formation is exclusively attributed to differences in the headgroup-substrate interaction.

To learn more about the energetics of the molecule–substrate interface in both SAMs, we have conducted dedicated exchange and S-SIMS experiments probing the relative stability of these SAMs. The experiments monitoring the exchange of the NC-NapS and NC-NapSe moieties in the respective SAMs on Au(111) by HDT molecules unambiguously demonstrated an almost complete exchange reaction for NC-NapS/Au(111) and a very small extent of this process, limited, presumably, to the defect sites only, in the case of NC-NapSe/Au(111). Considering that (i) both SAMs have similar structure and packing density and that (ii) the exchange process requires the complete removal of a SAM constituent by cleaving its bond to the substrate, we conclude a higher stability of the Se–Au bond as compared to the S–Au bond in these fully aromatic SAMs with either S or Se atoms directly attached to the aromatic backbones. Importantly, the same conclusion was reached in our previous exchange experiments where the relative stability of two homologue series of biphenyl-substituted alkanethiolates and alkaneselenolates (BPnS(Se): $CH_3-(C_6H_4)_2-(CH_2)_n-$S(Se), $n = 1-6$) on Au(111) was compared.[46] Thus, our present and previous[46] exchange experiments are complementary and show that, independent of the backbone character (aliphatic or aromatic), the Se–Au bond is more stable as compared to the S–Au one in the analogous SAMs.

To analyze the differences in stability of the molecule–substrate interface in the NC-NapS and NC-NapSe monolayers in more detail, we have exploited a novel approach based on the ion-induced desorption technique.[86,90] The resulting data (Figure 8) suggest that, whereas the ion-induced desorption of positive ions, associated with the complete molecule and following the breaking of the Au–S(Se) bond, is much more efficient for the NC-NapS SAMs, the emission of the positive ions related to desulfurized(deselenized) fragments by breaking the S(Se)–C bond is more efficient for the NC-NapSe monolayers. Following a general logic as well as the argument provided in our recent S-SIMS publication,[86] we assume that a larger efficiency of ion-induced cleavage of a given chemical bond is related to a smaller bond energy. Consequently, our S-SIMS data indicate higher stability of the Se–Au bond as compared to the S–Au one with, at the same time, lower stability of the adjacent Se–C bond as compared to the S–C one. Such effect of reversed relative stability of these two consecutive chemical bonds (*viz.* Au–S(Se) and S(Se)–C) can be understood intuitively considering that the valence electrons of the same S(Se) atom are involved in bonding with both the Au substrate and the naphthalene moiety. A larger involvement of the valence electrons of the S(Se) atom in one of these chemical bonds should result in a smaller involvement of these electrons in the second bond, reducing, consequently, the stability of the

latter. As documented by recent studies on the model system of BPnS(Se)/Au(111),[86] this intuitive explanation is also consistent with density functional theory (DFT) calculations of respective bond energies and molecular dynamics simulations of ion-induced desorption. A further hint is a comparison of thiolate-bonded molecules on Au, Ag, and Cu. C−S bond breaks more easily as the sulfur−metal bond gets stronger.[91,92] Summarizing this part and taking into account the literature data for the BPnS(Se) monolayers,[86] we can conclude that, independent of the character of the molecular backbone (aliphatic or aromatic), the Se−Au bond is more stable as compared to the S−Au one, with, however, lower stability of the adjacent C−Se bond as compared to that of C−S.

A reasonable question at this point is why, despite the stronger binding to the substrate in the case of Se headgroup, the respective SAMs adopt a structure dictated mostly by the intermolecular interaction, with a very simple unit cell, which is very similar to the molecular arrangement in crystalline naphthalene. This unit cell involves different adsorption sites for the identical molecules (see Figure 3e), thus indicating a presumably lower involvement of the molecule−substrate energetics into the 2D ordering. There are, however, two possible explanations of this seeming contradiction. First, it can be the effect of a lower corrugation of the binding energy surface for selenolates on Au(111) as compared to thiolates,[46] which is not necessarily related to the bond strength, as occurs for alkanethiolates that have a better mobility on Ag(111) compared to Au(111), in spite of the stronger bonding to the silver substrate.[1] Second, it can be an effect of the enhanced mobility of the gold atoms in the topmost layer of the substrate mediated by the strong bond to the adsorbate molecules in the case of the Se headgroup.[35,40,44] Indeed, it is well-known that the mobility of the atoms in the topmost layer of the substrate increases with increasing strength of the molecule−substrate bond due to the reduced interaction of the surface atoms with the underlying layers of the substrate.[46] This can then result in relaxation of the stress related to the formation of 2D incommensurate structure driven by the strong intermolecular interactions. However, the STM data for NC-NapSe/Au do not exhibit any evidence for a surface reconstruction since the molecular film, as a whole, mimics the structure of the nonreconstructed substrate, except for the small difference in the dimensions of the unit cells, related, presumably, to a limited accuracy of the STM measurements. Nevertheless, we think that the presented STM data do not allow a clear distinction between the lower corrugation and surface reconstruction scenarios, both of which are probably important.

The final part of our experiments was devoted to the analysis of the CT processes in the NC-NapS and NC-NapSe SAMs. According to the results of the dedicated RAES-CHC measurements, the characteristic CT time (τ_{CT}) between the terminal nitrile group of the assembled NC-NapS(Se) molecules and the Au(111) substrate is essentially identical (24 ± 4 fs) for both types of SAMs. This suggests very similar CT properties for the S−Au and Se−Au bonds, even though the entire τ_{CT} is mostly determined by the molecular backbone, with the CT through the backbone being the rate-limiting step.[57,58] Indeed, according to our previous results,[57,58] the characteristic CT time for the S−Au bond is just 2.3−2.8 fs as far as one can disentangle this contribution from the performance of the entire molecule.[58] Thus, a certain difference between the CT performance of the S−Au and Se−Au bonds cannot be excluded, but it is certainly much lower than the factor of ∼2.5 or even ∼10 in relation to the entire molecule as reported in the literature.[47,51] Note that this is the only way to deal with the charge transport/transfer properties of the S−Au and Se−Au bonds as to probe the respective molecular adsorbates as a whole and not just the S/Se−Au junction.

Significantly, the CT process in our case is related to individual molecules and does not depend on the packing density that is, however, quite close for the NC-NapS and NC-NapSe SAMs, excluding differences in matrix effects. It is also of importance that these molecules are the constituents of well-defined monolayers with similar structural and geometrical parameters. Note also that there are only a very limited number of experimental reports[47,51] which compare electron transport through SAMs based on sulfur and selenium analogues. These studies, reporting contradictory conclusions regarding either higher[51] or lower[47] conductance for the Se headgroup as compared to S one, use similar approaches based on analyzing apparent height differences in the STM images obtained for mixed SAMs of both types. Apart from the basic limitations of the applied methodology and possible role of defects, such mixed SAMs were certainly not as well-defined as the monolayers of the present study. Additional support comes from the most recent DFT calculations analyzing the influence of the S→Se headgroup substitution in biphenyl-based SAMs on gold ($C_6H_5-C_6H_4-S(Se)/Au(111)$).[22] These calculations show that gold substrate work function modification due to the SAM formation, as well as HOMO and LUMO level alignment, is essentially insensitive to the S→Se substitution, which is consistent with a similar CT efficiency observed for both types of SAMs in our experiments.

Following a recent line of arguments[48] connecting the strength of the S(Se)−Au bond with the overlap and involvement of the relevant electronic states, we get a link between the results of the experiments probing this bond strength (exchange and S-SIMS) with the conclusions regarding the CT properties of the SAM studied (RAES-CHC). Along these lines,

considering higher stability of the Au−Se bond compared to that of Au−S, concluded in our study, one would presumably expect noticeable differences in the CT properties. This was not observed in our RAES-CHC experiments, but at the same time, we demonstrated that the larger involvement of the headgroup atom in binding with the metal substrate occurs at the expense of the decreased involvement in the binding with the neighboring carbon atom. Since the tunneling process involves both C−S(Se) and S(Se)−Au bonds, we suppose that the better tunneling conditions in the latter case are compensated by the worse tunneling conditions in the former case. Thus, it looks as though the S→Se substitution causes a redistribution of the electronic states at the Au−S−C interface, which, on the average, does not change the total probability of charge carrier tunneling.

CONCLUSIONS

To understand the impact of the headgroup atom substitution on structure, stability, and charge transfer properties of SAMs, two representative model systems, NC-NapS/Au(111) and NC-NapSe/Au(111), were investigated.

As a starting point, we analyzed and compared in detail the structure and molecular organization in these monolayers using both microscopic and spectroscopic techniques. The SAMs were found to be of high quality and, what was particularly important in the context of the present study, possessed the same basic structural motif (close to $(2 \times 1.5\sqrt{3})$*rect*) as well as similar packing density (0.239 and 0.215 nm^2/molecule) and molecular orientation (a tilt angle of 41−42°). These characteristics allowed for rational comparison of the bond stability at the molecule−metal interface as well as for a comparison study of CT properties of thiolate and selenolate SAMs on noble metal substrates.

Consequently, by probing this interface by the dedicated exchange experiments and, independently, by S-SIMS technique, we demonstrated that the Au−Se bond is more stable than the Au−S one with, at the same time, lower stability of Se−C bond as compared to that of S−C, due to a redistribution of the electron density between these two adjacent bonds.

Finally, we probed the dynamic CT properties of the NC-NapS and NC-NapSe SAMs and found similar CT time for the both systems, which, in view of the well-defined monolayers with similar molecular organization and the single-molecule character of the CT process involved, suggest, in contrast to the previous studies, similar electronic coupling efficiency of the S and Se anchors.

Considering the bond stability as a measure of its strength and as a fingerprint for the overlap and involvement of the relevant electronic states, the exchange and S-SIMS results were correlated with the CT dynamics findings. Along these lines, consideration of the S−Au and Se−Au bonds alone leads, obviously, to a wrong conclusion regarding the electronic coupling efficiency of the S and Se anchors since the latter bond seems to be noticeably stronger. Instead, both S(Se)−Au and S(Se)−C bonds should be considered together. Since a comparably stronger Se−Au bond is accompanied by the weakening of the adjacent Se−C bond, the joint effect is comparable with the Au−S−C linker. This explains the equivalent CT dynamics properties of the NC-NapS and NC-NapSe SAMs found in this work and suggests that the S→Se substitution does not result in any improvement of the electronic coupling to the substrate. This observation of an independence of the CT properties on the exact interface chemistry goes in line with recently reported data for a different set of headgroup−substrate interactions.[93,94]

However, the S→Se substitution is certainly of importance for the molecular organization and structural perfection in the given SAMs. At least in the case of the aromatic SAMs, the Se−Au bond allows for a better structural perfection as compared to the thiolate anchor, resulting in monolayers of a higher quality.

METHODS

SAMs of chalcogenolates (thiolates, selenolates) are typically formed from the respective chalcogenols or the dichalcogenides. While aromatic thiols such as 6-cyanonaphthalene-2-thiol (NC-NapSH) are usually quite stable in air, the respective selenols easily oxidize. Based on the observation that selenoacetates can form well-ordered selenolate SAMs on Au(111) equally efficiently,[41] we used the air-stable 6-cyanonaphthalene-2-selenoacetate (NC-NapSeAc) as the SAM-forming molecule in this study. Due to the structural similarity, the two investigated molecules were prepared from a common intermediate, 2-bromo-6-cyanonaphthalene. This compound has been synthesized following a literature procedure,[95] starting from commercially available 2-bromo-6-naphthoic acid *via* the respective amide, which was dehydrated to the nitrile by action of trifluoroacetic acid anhydride (see Scheme S1 in the Supporting Information). Both, the bromoamide and the bromonitrile could be crystallized to obtain their solid-state structure (see the Supporting Information for details). The introduction of the selenium atom followed a recently reported protocol, which uses a sterically hindered silaselenol for the palladium-catalyzed formation of the C−Se bond.[96,97] The Se atom was then deprotected by the action of fluoride followed by a reprotection with acetyl chloride. A similar approach was used for the synthesis of the thiol compound by modifying previously developed protocols.[98−101] By using a silathiol, first C−S bond formation was achieved, followed by proton-induced S−Si bond cleavage. Both NC-NapSH and NC-NapSeAc turned out to be sufficiently air-stable to be handled under the typical SAM deposition conditions. Additional details can be found in the Supporting Information.

NapS used as a reference for the spectroscopic experiments and HDT used as substituent for the substitution experiments were purchased from Sigma-Aldrich and used as received. The NC-BPT and NC-TPT used as references for the spectroscopic

experiments were synthesized according to literature.[63] The substrates for the SAM preparation were purchased from Georg Albert PVD, Heidelberg, Germany. They represented epitaxial Au (99.99% purity) layers of 200 nm thickness, evaporated with a rate of 2 nm/s onto the mica slides held at 340 °C. The substrates were flame-annealed before immersion into solutions of the target compounds. This procedure yielded high-quality Au films with flat terraces of several 100 nm, exhibiting a (111) surface orientation with a typical surface reconstruction pattern.[102]

The NC-NapS and NC-NapSe SAMs were formed by immersion of freshly prepared gold substrates into a 1 mM solution of the above compounds in absolute ethanol for 24 h at room temperature (RT = 21 °C) or at elevated temperature (60 °C). After immersion, the SAM samples were carefully rinsed with the solvent, blown dry with argon, and either characterized immediately or kept for several days in argon-filled glass containers until the characterization at the synchrotron (see below). The reference NapS monolayers were fabricated in a similar fashion; the reference NC-BPT SAMs were prepared according to an established procedure.[58,64]

The fabricated films were characterized by STM, HRXPS, ellipsometry, IRRAS, NEXAFS spectroscopy, RAES, S-SIMS, and dedicated exchange experiments. All experiments were performed on the samples prepared at 60 °C because of their superior quality.

For ellipsometric characterization of the monolayers, a Sentech SE 400 ellipsometer with a He−Ne laser (wavelength 632.8 nm) was used. The angle of incidence was 70° with respect to the sample surface normal. The complex refractive indices of the Au substrates were measured before SAM deposition. The extinction coefficients and the refractive indices of the monolayers were assumed to be 0 and 1.55, respectively.

IR spectra of neat substances (reference) and SAMs were recorded using a Thermo Nicolet 6700 Fourier transform IR spectrometer purged with dried and CO_2-free air and equipped with a narrow band mercury cadmium telluride semiconductor detector. All spectra were recorded at 4 cm^{-1} resolution. Neat substance spectra were obtained using a single-reflection diamond attenuated total reflection unit. IRRAS of the SAMs was carried out with p-polarized radiation at 80° relative to the sample surface normal. Perdeuterated dodecanethiolate SAMs on gold served as reference for the IRRAS measurements. Since the C−D stretch bands interfered with the C≡N stretch signal of the samples, additional spectra were recorded with a nondeuterated HDT SAM as background. Vibrational mode assignments and identification of the TDM orientations were carried out with the help of DFT calculations of single molecules IR spectra at the BP86/SVP level.

STM measurements were carried out in air at room temperature using a MultiMode IIIa Digital Instruments microscope. In all cases, tips were prepared mechanically by cutting a 0.25 mm Pt/Ir alloy (8:2, Goodfellow) wire. The data were collected in constant current mode using tunneling currents in a range of 15−40 pA and a sample bias of 0.2−0.8 V (tip positive). No tip-induced changes were observed under these imaging conditions.

The HRXPS, NEXAFS, and RAES measurements were conducted at the MAX II storage ring at the MAX-IV laboratory in Lund, Sweden, using the bending magnet beamline D1011 (plane grating monochromator) and an experimental station equipped with a SCIENTA SES200 electron energy analyzer and a partial electron yield (PEY) detector. The experiments were carried out under UHV conditions at a base pressure $<1.5 \times 10^{-10}$ mbar. Special care, including a limited exposure of a particular spot as well as control measurements, was taken to avoid damage induced by X-rays.[68,103]

The HRXP spectra were collected in normal emission geometry for the Au 4f, Se 3d, S 2p, C 1s, and N 1s ranges. In addition, the O 1s range was monitored. The energy resolution was better than 100 meV (about 60 meV for most of the spectra), allowing a clear separation of individual spectral components. The BE scale of every spectrum was individually calibrated to the Au $4f_{7/2}$ emission line of the underlying Au substrate at 84.0 eV.[104] As far as this was necessary, the spectra were fitted by symmetric Voigt functions and a Shirley-type background. To fit the Se $3d_{5/2,3/2}$ and S $2p_{3/2,1/2}$ doublets, we used a pair of such peaks with the same fwhms values, branching ratios of 3:2 (Se $3d_{5/2}/3d_{3/2}$) and 2:1 (S $2p_{3/2}/2p_{1/2}$), and spin−orbit splittings (verified by fit) of ∼0.86 eV (Se $3d_{5/2}/3d_{3/2}$) and ∼1.18 eV (S $2p_{3/2}/2p_{1/2}$).[104]

The NEXAFS spectra were acquired at the carbon and nitrogen K-edges in the PEY acquisition mode with retarding voltages of −150 and −300 V, respectively. Linearly polarized synchrotron light with a polarization factor of ∼95% was used. The energy resolution was better than 100 meV. The incidence angle of X-rays was varied from 90° (*E* vector in the surface plane) to 20° (*E* vector near the surface normal) in steps of 10−20° to monitor the molecular orientation in the SAMs. This approach is based on the dependence of the cross section of the resonant photoexcitation process on the orientation of the electric field vector of the synchrotron light with respect to the molecular orbital of interest (so-called linear dichroism in X-ray absorption).[73] Raw NEXAFS spectra were normalized to the incident photon flux by division through a spectrum of a clean, freshly sputtered gold sample. Subsequently, the spectra were reduced to the standard form by subtracting a linear pre-edge background and normalizing to the unity edge jump (determined by a nearly horizontal plateau 40−50 eV above the respective absorption edges). The energy scale was calibrated by means of the most intense π^* resonance of highly oriented pyrolytic graphite at 285.38 eV[105] in combination with the well-known $\Delta h\nu \propto (h\nu)^{3/2}$ behavior of plane grating monochromators.[106] The resulting energy positions are expected to be accurate and reproducible within ±0.05 eV.

The RAES spectra were acquired at the N K-edge using a SCIENTA SES200 electron energy analyzer. The X-ray incidence angle was set to 55° to suppress orientational effects;[73,87] the take off angle of the electrons was close to normal emission. The resonant excitation energies were determined in the preliminary NEXAFS experiments. In addition, nonresonant Auger electron spectra were recorded at an excitation energy of 5−6 eV above the absorption edge. This setting seems to be optimal for nitrile-substituted SAMs on Au in order to maximize the signal-to-noise ratio and to avoid appearance of interfering gold photoemission in the spectra.[56] Finally, for every sample, a reference spectrum for the pre-edge excitation was measured. This spectrum was subtracted from the RAES and nonresonant AES spectra to correct them for a contribution of the photoemission, which could not be avoided completely.

The relative stability of the headgroup−substrate bonds in the NC-NapS and NC-NapSe monolayers was probed by dedicated exchange experiments. The above SAMs were immersed in the 1 mM ethanolic solution of HDT at room temperature. The progress of the exchange reaction was monitored for a given sample by the consecutive control of the advancing water contact angle. The measurements were carried out with a Rame-Hart goniometer, model 200, using ultrapure water (∼18 MΩ). The experiments were performed under ambient conditions (temperature = 21 °C, humidity = 25%), with the needle tip in contact with the drop. Averaged values of at least 50 measurements at different locations on each sample are reported.

The SIMS experiments were performed using a TOF SIMS V system (ION TOF GmbH, Germany). The instrument was operated at a base pressure of 6×10^{-10} mbar. The primary 30 keV Bi^+ ion beam was scanned over a 500 μm × 500 μm area during the data acquisition. All spectra were collected in the static SIMS regime using a total ion dose of up to 8×10^{10} ions/cm^2 which, for these kinds of SAMs, ensures analysis with negligible ion-induced damage, as documented by our previous studies.[107] The secondary ions were extracted into a reflectron time-of-flight mass spectrometer before reaching the MCP detector. For each type of SAM, three different areas on three different samples were examined with a reproducibility of ∼10% in the peak intensities. Before analysis, all spectra were normalized to the respective total count numbers.

Conflict of Interest: The authors declare no competing financial interest.

Supporting Information Available: Synthetic details for the NC-NapS and NC-NapSe precursors, X-ray structures of some intermediates, tabulated IR data, and representative SIMS

spectra for the NC-NapS and NC-NapSe SAMs on Au(111). This material is available free of charge *via* the Internet at http://pubs.acs.org.

Acknowledgment. We thank the Max-IV staff, and A. Preobrajenski, in particular, for the technical support during the synchrotron-based experiments, as well as Prof. Marek Szymonski for providing access to the STM at the Department of Physics of Nanostructures and Nanotechnology at the Jagiellonian University. This work was supported financially by the Deutsche Forschungsgemeinschaft (Grants ZH 63/14-2 and MAP B.1.4), the National Science Centre Poland (Grant DEC-2013/10/E/ST5/00060), and by funding from the European Community's Seventh Framework Programme (FP7/2007-2013) CALIPSO under Grant Agreement No. 312284. The S-SIMS equipment was purchased with the financial support of the European Regional Development Fund (Grant POIG.02.02.00-12-023/08). We also wish to acknowledge the generous gifts of gold by Umicore, Hanau, Germany, and trifluoroacetic anhydride by Solvay Fluor GmbH, Hannover, Germany.

REFERENCES AND NOTES

1. Ulman, A. Formation and Structure of Self-Assembled Monolayers. *Chem. Rev.* **1996**, *96*, 1533–1554.
2. Schreiber, F. Self-Assembled Monolayers: From 'Simple' Model Systems to Biofunctionalized Interfaces. *J. Phys.: Condens. Matter* **2004**, *16*, R881–R900.
3. Love, J. C.; Estroff, L. A.; Kriebel, J. K.; Nuzzo, R. G.; Whitesides, G. M. Self-Assembled Monolayers of Thiolates on Metals as a Form of Nanotechnology. *Chem. Rev.* **2005**, *105*, 1103–1169.
4. Schreiber, F. Structure and Growth of Self-Assembling Monolayers. *Prog. Surf. Sci.* **2000**, *65*, 151–256.
5. McGuiness, C. L.; Diehl, G. A.; Blasini, D.; Smilgies, D.-M.; Zhu, M.; Samarath, N.; Weidner, T.; Ballav, N.; Zharnikov, M.; Allara, D. L. Molecular Self-Assembly at Bare Semiconductor Surfaces: Cooperative Substrate-Molecule Effects in Octadecanethiolate Monolayer Assemblies on GaAs (111), (110), and (100). *ACS Nano* **2010**, *4*, 3447–3465.
6. Fenter, P.; Eisenberger, P.; Liang, K. S. Chain-Length Dependence of the Structures and Phases of $CH_3(CH_2)_{n-1}SH$ Self-Assembled on Au(111). *Phys. Rev. Lett.* **1993**, *70*, 2447–2450.
7. Fenter, P.; Eberhardt, A.; Eisenberger, P. Self-Assembly of *n*-Alkyl Thiols as Disulfides on Au(111). *Science* **1994**, *266*, 1216–1218.
8. Poirier, G. E.; Tarlov, M. J. The c(4 × 2) Superlattice of *n*-Alkanethiol Monolayers Self-Assembled on Au(111). *Langmuir* **1994**, *10*, 2853–2856.
9. Leung, T. Y. B.; Schwartz, P.; Scoles, G.; Schreiber, F.; Ulman, A. Structure and Growth of 4-Methyl-4′-mercaptobiphenyl Monolayers on Au(111): A Surface Diffraction Study. *Surf. Sci.* **2000**, *458*, 34–52.
10. Fuxen, C.; Azzam, W.; Arnold, R.; Witte, G.; Terfort, A.; Wöll, C. Structural Characterization of Organothiolate Adlayers on Gold: The Case of Rigid, Aromatic Backbones. *Langmuir* **2001**, *17*, 3689–3695.
11. Ishida, T.; Mizutani, W.; Azehara, H.; Sato, F.; Choi, N.; Akiba, U.; Fujihira, M.; Tokumoto, H. Adsorption Processes of Self-Assembled Monolayers Made from Terphenyl Thiols. *Langmuir* **2001**, *17*, 7459–7463.
12. Azzam, W.; Fuxen, C.; Birkner, A.; Rong, H.-T.; Buck, M.; Wöll, Ch. Coexistence of Different Structural Phases in Thioaromatic Monolayers on Au(111). *Langmuir* **2003**, *19*, 4958–4968.
13. Bashir, A.; Azzam, W.; Rohwerder, M.; Terfort, A. Polymorphism in Self-Assembled Terphenylthiolate Monolayers on Au(111). *Langmuir* **2013**, *29*, 13449–13456.
14. Fenter, P.; Eisenberger, P.; Li, J.; Camillone, N., III; Bernasek, S.; Scoles, G.; Ramanarayanan, T. A.; Liang, K. S. Structure of Octadecyl Thiol Self-Assembled on the Silver(111) Surface: An Incommensurate Monolayer. *Langmuir* **1991**, *7*, 2013–2016.
15. Rieley, H.; Kendall, G. K.; Jones, R. G.; Woodruff, P. X-ray Studies of Self-Assembled Monolayers on Coinage Metals. 2. Surface Adsorption Structures in 1-Octanethiol on Cu(111) and Ag(111) and their Determination by the Normal Incidence X-ray Standing Wave Technique. *Langmuir* **1999**, *15*, 8856–8866.
16. Zharnikov, M.; Frey, S.; Rong, H.; Yang, Y. J.; Heister, K.; Buck, M.; Grunze, M. The Effect of Sulfur-Metal Bonding on the Structure of Self-Assembled Monolayers. *Phys. Chem. Chem. Phys.* **2000**, *2*, 3359–3362.
17. Rong, H. T.; Frey, S.; Yang, Y. J.; Zharnikov, M.; Buck, M.; Wühn, M.; Wöll, Ch.; Helmchen, G. On the Importance of the Headgroup Substrate Bond in Thiol Monolayers: A Study of Biphenyl-Based Thiols on Gold and Silver. *Langmuir* **2001**, *17*, 1582–1593.
18. Shaporenko, A.; Brunnbauer, M.; Terfort, A.; Grunze, M.; Zharnikov, M. Structural Forces in Self-Assembled Monolayers: Terphenyl-Substituted Alkanethiols on Noble Metal Substrates. *J. Phys. Chem. B* **2004**, *108*, 14462–14469.
19. Shaporenko, A.; Müller, J.; Weidner, T.; Terfort, A.; Zharnikov, M. Balance of Structure-Building Forces in Selenium-Based Self-Assembled Monolayers. *J. Am. Chem. Soc.* **2007**, *129*, 2232–2233.
20. von Wrochem, F.; Gao, D.; Scholz, F.; Nothofer, H.-G.; Nelles, G.; Wessels, J. M. Efficient Electronic Coupling and Improved Stability with Dithiocarbamate-Based Molecular Junctions. *Nat. Nanotechnol.* **2010**, *5*, 618–624.
21. Karthäuser, S. Control of Molecule-Based Transport for Future Molecular Devices. *J. Phys.: Condens. Matter* **2011**, *23*, 1–16.
22. Heimel, G.; Romaner, L.; Zojer, E.; Bredas, J.-L. Toward Control of the Metal-Organic Interfacial Electronic Structure in Molecular Electronics: A First-Principles Study on Self-Assembled Monolayers of π-Conjugated Molecules on Noble Metals. *Nano Lett.* **2007**, *7*, 932–940.
23. Weidner, T.; Shaporenko, A.; Müller, J.; Höltig, M.; Terfort, A.; Zharnikov, M. Self-Assembled Monolayers of Aromatic Tellurides on (111)-Oriented Gold and Silver Substrates. *J. Phys. Chem. C* **2007**, *111*, 11627–11635.
24. Samant, M. G.; Brown, C. A.; Gordon, J. G., II. Formation of an Ordered Self-Assembled Monolayer of Docosaneselenol on Gold(111)-Structure by Surface X-ray-Diffraction. *Langmuir* **1992**, *8*, 1615–1618.
25. Dishner, M. H.; Hemminger, J. C.; Feher, F. J. Scanning Tunneling Microscopy Characterization of Organoselenium Monolayers on Au(111). *Langmuir* **1997**, *13*, 4788–4790.
26. Bandyopadhyay, K.; Vijayamohanan, K. Formation of a Self-Assembled Monolayer of Diphenyl Diselenide on Polycrystalline Gold. *Langmuir* **1998**, *14*, 625–629.
27. Huang, F. K.; Horton, R. C., Jr.; Myles, D. C.; Garrell, R. L. Selenolates as Alternatives to Thiolates for Self-Assembled Monolayers: A SERS Study. *Langmuir* **1998**, *14*, 4802–4808.
28. Bandyopadhyay, K.; Vijayamohanan, K.; Venkataramanan, M.; Pradeep, T. Self-Assembled Monolayers of Small Aromatic Disulfide and Diselenide Molecules on Polycrystalline Gold Films: A Comparative Study of the Geometrical Constraint Using Temperature-Dependent Surface-Enhanced Raman Spectroscopy, X-ray Photoelectron Spectroscopy, and Electrochemistry. *Langmuir* **1999**, *15*, 5314–5322.
29. Nakano, K.; Sato, T.; Tazaki, M.; Takagi, M. Self-Assembled Monolayer Formation from Decaneselenol on Polycrystalline Gold As Characterized by Electrochemical Measurements, Quartz-Crystal Microbalance, XPS, and IR Spectroscopy. *Langmuir* **2000**, *16*, 2225–2229.
30. Han, S. W.; Lee, S. J.; Kim, K. Self-Assembled Monolayers of Aromatic Thiol and Selenol on Silver: Comparative Study of Adsorptivity and Stability. *Langmuir* **2001**, *17*, 6981–6987.
31. Yee, C. K.; Ulman, A.; Ruiz, J. D.; Parikh, A.; White, H.; Rafailovich, M. Alkyl Selenide- and Alkyl Thiolate-Functionalized

Gold Nanoparticles: Chain Packing and Bond Nature. *Langmuir* **2003**, *19*, 9450–9458.
32. Monnell, J. D.; Stapleton, J. J.; Jackiw, J. J.; Dunbar, T.; Reinerth, W. A.; Dirk, S. M.; Tour, J. M.; Allara, D. L.; Weiss, P. S. Ordered Local Domain Structures of Decaneselenolate and Dodecaneselenolate Monolayers on Au{111}. *J. Phys. Chem. B* **2004**, *108*, 9834–9841.
33. Sato, Y.; Mizutani, F. Formation and Characterization of Aromatic Selenol and Thiol Monolayers on Gold: *In-Situ* IR Studies and Electrochemical Measurements. *Phys. Chem. Chem. Phys.* **2004**, *6*, 1328–1331.
34. Shaporenko, A.; Ulman, A.; Terfort, A.; Zharnikov, M. Self-Assembled Monolayers of Alkaneselenols on (111) Gold and Silver. *J. Phys. Chem. B* **2005**, *109*, 3898–3906.
35. Shaporenko, A.; Cyganik, P.; Buck, M.; Terfort, A.; Zharnikov, M. Self-Assembled Monolayers of Aromatic Selenols on Noble Metal Substrates. *J. Phys. Chem. B* **2005**, *109*, 13630–13638.
36. Shaporenko, A.; Cyganik, P.; Buck, M.; Ulman, A.; Zharnikov, M. Self-Assembled Monolayers of Semifluorinated Alkaneselenolates on Noble Metal Substrates. *Langmuir* **2005**, *21*, 8204–8213.
37. Käfer, D.; Bashir, A.; Witte, G. J. Interplay of Anchoring and Ordering in Aromatic Self-Assembled Monolayers. *Phys. Chem. C* **2007**, *111*, 10546–10551.
38. Weidner, T.; Shaporenko, A.; Ballav, N.; Ulman, A.; Zharnikov, M. Modification of Alkaneselenolate Monolayers by Low-Energy Electrons. *J. Phys. Chem. C* **2008**, *112*, 1191–1198.
39. Weidner, T.; Shaporenko, A.; Müller, J.; Schmid, M.; Cyganik, P.; Terfort, A.; Zharnikov, M. The Effect of the Bending Potential on Molecular Arrangement in Alkaneselenolate Self-Assembled Monolayers. *J. Phys. Chem. C* **2008**, *112*, 12495–12506.
40. Cyganik, P.; Szelągowska-Kunstman, K.; Terfort, A.; Zharnikov, M. Odd-Even Effect in Molecular Packing of Biphenyl-Substituted Alkaneselenolate Self-Assembled Monolayers on Au(111)—Scanning Tunnelling Microscopy Study. *J. Phys. Chem. C* **2008**, *112*, 15466–15473.
41. Bashir, A.; Käfer, D.; Müller, J.; Wöll, C.; Terfort, A.; Witte, G. Selenium as a Key Element for Highly Ordered Aromatic Self-Assembled Monolayers. *Angew. Chem., Int. Ed.* **2008**, *47*, 5250–5252.
42. Track, A. M.; Rissner, F.; Heimel, G.; Romaner, L.; Käfer, D.; Bashir, A.; Rangger, G. M.; Hofmann, O. T.; Bucko, T.; Witte, G.; et al. Simultaneously Understanding the Geometric and Electronic Structure of Anthraceneselenolate on Au(111): A Combined Theoretical and Experimental Study. *J. Phys. Chem. C* **2010**, *114*, 2677–2684.
43. Hohman, J. N.; Kim, M.; Schüpbach, B.; Kind, M.; Thomas, J. C.; Terfort, A.; Weiss, P. S. The Dynamic Double Lattice of 1-Adamantaneselenolate Self-Assembled Monolayers on Au{111}. *J. Am. Chem. Soc.* **2011**, *133*, 19422–19431.
44. Dendzik, M.; Terfort, A.; Cyganik, P. Odd—Even Effect in the Polymorphism of Self-Assembled Monolayers of Biphenyl-Substituted Alkaneselenolates on Au(111). *J. Phys. Chem. C* **2012**, *116*, 19535–19542.
45. Hohman, J. N.; Thomas, J. C.; Zhao, Y.; Auluck, H.; Kim, M.; Vijselaar, W.; Kommeren, S.; Terfort, A.; Weiss, P. S. Exchange Reactions between Alkanethiolates and Alkaneselenols on Au{111}. *J. Am. Chem. Soc.* **2014**, *136*, 8110–8121.
46. Szelagowska-Kunstman, K.; Cyganik, P.; Schüpbach, B.; Terfort, A. Relative Stability of Thiol and Selenol Based SAMs on Au(111) - Exchange Experiments. *Phys. Chem. Chem. Phys.* **2010**, *12*, 4400–4406.
47. Monnell, J. D.; Stapleton, J. J.; Dirk, S. M.; Reinerth, W. A.; Tour, J. M.; Allara, D. L.; Weiss, P. S. Relative Conductances of Alkaneselenolate and Alkanethiolate Monolayers on Au(111). *J. Phys. Chem. B* **2005**, *109*, 20343–20349.
48. Yokota, K.; Taniguchi, M.; Kawai, T. Control of Electrode—Molecule Interface for Molecular Devices. *J. Am. Chem. Soc.* **2007**, *129*, 5818–5619.
49. Di Ventra, M.; Lang, N. D. Transport in Nanoscale Conductors from First Principles. *Phys. Rev. B* **2001**, *65*, 045402.
50. Di Ventra, M.; Lang, N. D.; Pantelides, S. T. Electronic Transport in Single Molecules. *Chem. Phys.* **2002**, *281*, 189–198.
51. Patrone, L.; Palacin, S.; Charlier, J.; Armand, F.; Bourgoin, J. P.; Tang, H.; Gauthier, S. Evidence of the Key Role of Metal—Molecule Bonding in Metal—Molecule—Metal Transport Experiments. *Phys. Rev. Lett.* **2003**, *91*, 096802.
52. Brühwiler, P. A.; Karis, O.; Mårtensson, N. Charge-Transfer Dynamics Studied Using Resonant Core Spectroscopies. *Rev. Mod. Phys.* **2002**, *74*, 703–740.
53. Schnadt, J.; Brühwiler, P. A.; Patthey, L.; O'Shea, J. N.; Södergen, S.; Odelius, M.; Ahuja, R.; Karis, O.; Bässler, M.; Persson, P.; et al. Experimental Evidence for Sub-3-fs Charge Transfer from an Aromatic Adsorbate to a Semiconductor. *Nature* **2002**, *418*, 620–623.
54. de Jong, M. P.; Friedlein, R.; Sorensen, S. L.; Öhrwall, G.; Osikowicz, W.; Tengsted, C. Orbital-Specific Dynamic Charge Transfer from Fe(II)-tetraphenylporphyrin Molecules to Molybdenum Disulfide Substrates. *Phys. Rev. B* **2005**, *72*, 035448.
55. Föhlisch, A.; Feulner, P.; Hennies, F.; Fink, A.; Menzel, D.; Sanchez-Portal, D.; Echenique, P. M.; Wurth, W. Direct Observation of Electron Dynamics in the Attosecond Domain. *Nature* **2005**, *436*, 373–376.
56. Neppl, S.; Bauer, U.; Menzel, D.; Feulner, P.; Shaporenko, A.; Zharnikov, M.; Kao, P.; Allara, D. Charge Transfer Dynamics in Self-Assembled Monomolecular Films. *Chem. Phys. Lett.* **2007**, *447*, 227–231.
57. Kao, P.; Neppl, S.; Feulner, P.; Allara, D. L.; Zharnikov, M. Charge Transfer Time in Alkanethiolate Self-Assembled Monolayers *via* Resonant Auger Electron Spectroscopy. *J. Phys. Chem. C* **2010**, *114*, 13766–13773.
58. Hamoudi, H.; Neppl, S.; Kao, P.; Schüpbach, B.; Feulner, P.; Terfort, A.; Allara, D.; Zharnikov, M. Orbital-Dependent Charge Transfer Dynamics in Conjugated Self-Assembled Monolayers. *Phys. Rev. Lett.* **2011**, *107*, 027804-1–027801-4.
59. Blobner, F.; Coto, P. B.; Allegretti, F.; Bockstedte, M.; Rubio-Pons, O.; Wang, H.; Allara, D. L.; Zharnikov, M.; Thoss, M.; Feulner, P. Orbital Symmetry Dependent Electron Transfer through Molecules Assembled on Metal Substrates. *J. Phys. Chem. Lett.* **2012**, *3*, 436–440.
60. Caprioli, F.; Decker, F. A New Simple Method To Heal Defects and To Improve Electrode Passivity of Aromatic SAMs on Gold. *J. Electroanal. Chem.* **2013**, *708*, 68–72.
61. Ganesh, V.; Lakshminarayanan, V. Scanning Tunneling Microscopy, Fourier Transform Infrared Spectroscopy, and Electrochemical Characterization of 2-Naphthalenethiol Self-Assembled Monolayers on the Au Surface: A Study of Bridge-Mediated Electron Transfer in $Ru(NH_3)_6^{2+}/Ru(NH_3)_6^{3+}$ Redox Reactions. *J. Phys. Chem. B* **2005**, *109*, 16372–16381.
62. Jiang, P.; Nion, A.; Marchenko, A.; Piot, L.; Fichou, D. Rotational Polymorphism in 2-Naphthalenethiol SAMs on Au(111). *J. Am. Chem. Soc.* **2006**, *128*, 12390–12391.
63. Ballav, N.; Schüpbach, B.; Dethloff, O.; Feulner, P.; Terfort, A.; Zharnikov, M. Direct Probing Molecular Twist and Tilt in Aromatic Self-Assembled Monolayers. *J. Am. Chem. Soc.* **2007**, *129*, 15416–15417.
64. Ballav, N.; Schüpbach, B.; Neppl, S.; Feulner, P.; Terfort, A.; Zharnikov, M. Biphenylnitrile-Based Self-Assembled Monolayers on Au(111): Spectroscopic Characterization and Resonant Excitation of the Nitrile Tail Group. *J. Phys. Chem. C* **2010**, *114*, 12719–12727.
65. Ponomarev, V. I.; Filipenko, O. S.; Atovmyan, L. O. Crystal and Molecular—Structure of Naphthalene at −150 Degrees Celsius. *Kristallografiya* **1976**, *21*, 392–394.
66. Laibinis, P. E.; Whitesides, G. M.; Allara, D. L.; Tao, Y. T.; Parikh, A. N.; Nuzzo, R. G. Comparison of the Structures and Wetting Properties of Self-Assembled Monolayers of *N*-Alkanethiols on the Coinage Metal Surfaces, Cu, Ag, Au. *J. Am. Chem. Soc.* **1991**, *113*, 7152–7167.
67. Zharnikov, M.; Grunze, M. Spectroscopic Characterization of Thiol-Derived Self-Assembled Monolayers. *J. Phys.: Condens. Matter* **2001**, *13*, 11333–11365.

68. Zharnikov, M. High-Resolution X-ray Photoelectron Spectroscopy in Studies of Self-Assembled Organic Monolayer. *J. Electron Spectrosc. Relat. Phenom.* **2010**, *178*−*179*, 380–393.
69. Hamoudi, H.; Kao, P.; Nefedov, A.; Allara, D. L.; Zharnikov, M. X-ray Spectroscopy Characterization of Self-Assembled Monolayers of Nitrile-Substituted Oligo(phenylene ethynylene)s with Variable Chain Length. *Beilstein J. Nanotechnol.* **2012**, *3*, 12–24.
70. Thome, J.; Himmelhaus, M.; Zharnikov, M.; Grunze, M. Increased Lateral Density in Alkanethiolate Films on Gold by Mercury Adsorption. *Langmuir* **1998**, *14*, 7435–7449.
71. Waske, P.; Wächter, T.; Terfort, A.; Zharnikov, M. Nitro-Substituted Aromatic Thiolate Self-Assembled Monolayers: Structural Properties and Electron Transfer upon Resonant Excitation of the Tail Group. *J. Phys. Chem. C* **2014**, *118*, 26049–26060.
72. Greenler, R. G. Infrared Study of Adsorbed Molecules on Metal Surfaces by Reflection Techniques. *J. Chem. Phys.* **1966**, *44*, 310–315.
73. Stöhr, J. *NEXAFS Spectroscopy*; Springer-Verlag: Berlin, 1992.
74. Horsley, J.; Stöhr, J.; Hitchcock, A. P.; Newbury, D. C.; Johnson, A. L.; Sette, F. Resonances in the K-Shell Excitation Spectra of Benzene and Pyridine: Gas Phase, Solid and Chemisorbed States. *J. Chem. Phys.* **1985**, *83*, 6099–6107.
75. Yokoyama, T.; Seki, K.; Morisada, I.; Edamatsu, K.; Ohta, T. X-ray Absorption Spectra of Poly-*p*-phenylenes and Polyacenes: Localization of π^* Orbitals. *Phys. Scr.* **1990**, *41*, 189–192.
76. Frey, S.; Stadler, V.; Heister, K.; Eck, W.; Zharnikov, M.; Grunze, M.; Zeysing, B.; Terfort, A. Structure of Thioaromatic Self-Assembled Monolayers on Gold and Silver. *Langmuir* **2001**, *17*, 2408–2415.
77. Robin, M. B.; Ishii, I.; McLaren, R.; Hitchcock, A. P. Fluorination Effects on the Inner-Shell Spectra of Unsaturated Molecules. *J. Electron Spectrosc. Relat. Phenom.* **1988**, *47*, 53–92.
78. Ågren, H.; Vahtras, O.; Carravetta, V. Near-Edge Core Photoabsorption in Polyacenes: Model Molecules for Graphite. *Chem. Phys.* **1995**, *196*, 47–58.
79. Oji, H.; Mitsumoto, R.; Ito, E.; Ishii, H.; Ouchi, Y.; Seki, K.; Yokoyama, T.; Ohta, T.; Kosugi, N. Core Hole Effect in NEXAFS Spectroscopy of Polycyclic Aromatic Hydrocarbons: Benzene, Chrysene, Perylene, and Coronene. *J. Chem. Phys.* **1998**, *109*, 10409–10418.
80. Dauselt, J.; Zhao, J.; Kind, M.; Binder, R.; Bashir, A.; Terfort, A.; Zharnikov, M. Compensation of the Odd−Even Effects in Araliphatic Self-Assembled Monolayers by Non-symmetric Attachment of the Aromatic Part. *J. Phys. Chem. C* **2011**, *115*, 2841–2854.
81. Rangan, S.; Gallet, J.-J.; Bournel, F.; Kubsky, S.; Le Guen, K.; Dufour, G.; Rochet, F.; Sirotti, F.; Carniato, S.; Ilakovac, V. Adsorption of Benzonitrile on Si(001)−2 × 1 at 300 K. *Phys. Rev. B* **2005**, *71*, 165318-1–165318-12.
82. Carniato, S.; Ilakovac, V.; Gallet, J.-J.; Kukk, E.; Luo, Y. Hybrid Density-Functional Theory Calculations of Near-Edge X-ray Absorption Fine-Structure Spectra: Applications on Benzonitrile in Gas Phase. *Phys. Rev. A* **2005**, *71*, 022511.
83. Hautman, J.; Bareman, J. P.; Mar, W.; Klein, M. L. Molecular Dynamics Investigations of Self-Assembled Monolayers. *J. Chem. Soc., Faraday Trans.* **1991**, *87*, 2031–2037.
84. Frey, S.; Shaporenko, A.; Zharnikov, M.; Harder, P.; Allara, D. L. Self-Assembled Monolayers of Nitrile-Functionalized Alkanethiols on Gold and Silver Substrates. *J. Phys. Chem. B* **2003**, *107*, 7716–7725.
85. Cassie, A. B. D.; Baxter, S. Wettability of Porous Surfaces. *Trans. Faraday Soc.* **1944**, *40*, 546–551.
86. Ossowski, J.; Rysz, J.; Krawiec, M.; Maciazek, D.; Postawa, Z.; Terfort, A.; Cyganik, P. Oscillations in the Stability of Chemical Bonds Revealed by Ion-Induced Desorption. *Angew. Chem., Int. Ed.* **2015**, *54*, 1336–1340.
87. Piancastelli, M. N. Auger Resonant Raman Studies of Atoms and Molecules. *J. Electron Spectrosc. Relat. Phenom.* **2000**, *107*, 1–26.
88. Kempgens, B.; Kivimäki, A.; Neeb, M.; Köppe, H. M.; Bradschaw, A. M.; Feldhaus, J. A High-Resolution N 1s Photoionization Study of the N_2 Molecule in the Near-Threshold Region. *J. Phys. B* **1996**, *29*, 5389–5403.
89. Wurth, W.; Föhlisch, A. *Direct Observation of Electron Dynamics at Surfaces Using X-ray Spectroscopy*; Ultrafast Phenomena XV. Springer Series in Chemical Physics; Springer-Verlag: Berlin, 2007; Vol. 88, pp 707−709.
90. Wyczawska, S.; Cyganik, P.; Terfort, A.; Lievens, P. Ion-Beam-Induced Desorption as a Method for Probing the Stability of the Molecule−Substrate Interface in Self-Assembled Monolayers. *ChemPhysChem* **2011**, *12*, 2554–2557.
91. Konopka, M.; Rousseau, R.; Stich, I.; Marx, D. Detaching Thiolates from Copper and Gold Clusters: Which Bonds To Break? *J. Am. Chem. Soc.* **2004**, *126*, 12103–12111.
92. Konopka, M.; Rousseau, R.; Stich, I.; Marx, D. Electronic Origin of Disorder and Diffusion at a Molecule−Metal Interface: Self-Assembled Monolayers of CH_3S on Cu(111). *Phys. Rev. Lett.* **2005**, *95*, 096102.
93. Liao, K.-C.; Yoon, H. J.; Bowers, C. M.; Simeone, F. C.; Whitesides, G. M. Replacing $Ag^{TS}SCH_2$-R with $Ag^{TS}O_2C$-R in EGaIn-Based Tunneling Junctions Does Not Significantly Change Rates of Charge Transport. *Angew. Chem., Int. Ed.* **2014**, *53*, 3889–3893.
94. Bowers, C. M.; Liao, K.-C.; Zaba, T.; Rappoport, D.; Baghbanzadeh, M.; Breiten, B.; Krzykawska, A.; Cyganik, P.; Whitesides, G. M. Characterizing the Metal−SAM Interface in Tunneling Junctions. *ACS Nano* **2015**, *9*, 1471–1477.
95. Allan, M.; Chamon, S.; Hu, Q.-Y.; Imase, H.; Papillon, J. Arylpyridine Derivatives as Aldosterone Synthase Inhibitors. Patent WO 2011/061168, 2011.
96. Grenader, K.; Schüpbach, B.; Peters, A.; Kümmel, O.; Halter, O.; Terfort, A. Catalytic C-Se Bond Formation under Very Mild Conditions for the Two-Step, One-Pot Synthesis of Arylselenoacetates. *Adv. Synth. Catal.* **2012**, *354*, 2653–2658.
97. Grenader, K.; Kind, M.; Silies, L.; Peters, A.; Bats, J. W.; Bolte, M.; Terfort, A. Structural Characterization of a Series of Aryl Selenoacetates. *J. Mol. Struct.* **2013**, *1039*, 61–70.
98. Rane, A. M.; Miranda, E. I.; Soderquist, J. A. Potassium Triisopropylsilanethiolate: Vinyl and Aryl Sulfides through Pd Catalyzed Cross Coupling. *Tetrahedron Lett.* **1994**, *35*, 3225–3226.
99. Fernandez-Rodriguez, M. A.; Shen, Q. L.; Hartwig, J. F. A General and Long-Lived Catalyst for the Palladium-Catalyzed Coupling of Aryl Halides with Thiols. *J. Am. Chem. Soc.* **2006**, *128*, 2180–2181.
100. Hartwig, J. F. Evolution of a Fourth Generation Catalyst for the Amination and Thioetherification of Aryl Halides. *Acc. Chem. Res.* **2008**, *41*, 1534–1544.
101. Fernandez-Rodriguez, M. A.; Hartwig, J. F. A General and Long-Lived Catalyst for the Palladium-Catalyzed Coupling of Aryl Halides with Thiols. *Chem.—Eur. J.* **2010**, *16*, 2355–2359.
102. Satterley, C. J.; Lovelock, K. R. J.; Thom, I.; Dhanak, V. R.; Buck, M.; Jones, R. G. Normal Incidence X-ray Standing Wave Analysis of Thin Gold Films. *Surf. Sci.* **2006**, *600*, 4825–4828.
103. Heister, K.; Zharnikov, M.; Grunze, M.; Johansson, L. S. O.; Ulman, A. Characterization of X-ray Induced Damage in Alkanethiolate Monolayers by High-Resolution Photoelectron Spectroscopy. *Langmuir* **2001**, *17*, 8–11.
104. Moulder, J. F.; Stickle, W. E.; Sobol, P. E.; Bomben, K. D. In *Handbook of X-ray Photoelectron Spectroscopy*l Chastian, J., Ed.; Perkin-Elmer Corp.: Eden Prairie, MN, 1992.
105. Batson, P. E. Carbon-1s Near-Edge-Absorption Fine-Structure in Graphite. *Phys. Rev. B* **1993**, *48*, 2608–2610.
106. Domke, M.; Mandel, T.; Puschmann, A.; Xue, C.; Shirley, D. A.; Kaindl, G.; Petersen, H.; Kuske, P. Performance of the

High-Resolution SX700/II Monochromator. *Rev. Sci. Instrum.* **1992**, *63*, 80–89.
107. Cyganik, P.; Vandeweert, E.; Postawa, Z.; Bastiaansen, J.; Vervaecke, F.; Lievens, P.; Silverans, R. E.; Winograd, N. Modification and Stability of Aromatic Self-Assembled Monolayers upon Irradiation with Energetic Particles. *J. Phys. Chem. B* **2005**, *109*, 5085–5094.